

Impact of Josephson Junction Array modes on Fluxonium Readout

Shraddha Singh^{1,2,3,*} Emma Rosenfeld^{3,†} Gil Refael^{4,3} and Aashish Clerk^{5,3}

¹*Department of Applied Physics and Physics, Yale University, New Haven, Connecticut 06511, USA*

²*Yale Quantum Institute, Yale University, New Haven, Connecticut 06511, USA*

³*Amazon Web Services, Pasadena 91001, California, USA*

⁴*California Institute of Technology, Pasadena 91001, California, USA*

⁵*University of Chicago, Illinois, USA*

(Dated: September 23, 2024)

Fluxonium qubits, known for their high coherence and fast gates, are a promising candidate for superconducting architectures. High-fidelity measurement of these qubits is a crucial component in employing a fluxonium-based architecture for fault-tolerant quantum computing. We present an analysis of dispersive readout in fluxonium qubits, specifically considering the ‘parasitic’ internal modes of a Josephson junction array (JJA) which constitutes the inductive shunt in the circuit. Measurement of superconducting circuits is currently limited by state transitions in the qubit, when increasing photons in the readout mode, also known as measurement-induced state transitions (MIST). Our analysis reveals that coupling to the parasitic modes of JJA introduces additional state transitions during fluxonium readout. Consequently, such parasitic-mode-assisted MIST effects, which we refer to as p-MIST, can lower the onset of MIST effects to as low as ~ 10 average photons in the readout mode, severely impacting the readout performance. We verify that a significant number of these parasitic transitions, mediated by the coupling of the parasitic mode to the qubit mode, occur with considerable rates. The residual population in the parasitic modes from p-MIST also causes significant dephasing of the fluxonium qubit. We extend our findings across various fluxonium circuits, analyzing the dependency of qubit-parasitic mode coupling on different circuit parameters. Our results underscore the substantial impact parasitic modes can have on the readout fidelity and coherence of highly anharmonic superconducting circuits.

I. INTRODUCTION

The fluxonium circuit, a Josephson junction shunted by an inductor and a capacitor, is a promising qubit due to its large anharmonicity, flexible parameters, and long lifetimes [1–4]. Recent high-fidelity single- [5] and two-qubit [6, 7] gate demonstrations show error probabilities of $\sim 10^{-4}$ and $\sim 10^{-3}$, respectively, which likely can be improved further [8–12]. For this work, we assume that the inductive shunt in a fluxonium circuit constitutes a Josephson junction array (JJA) [13, 14] due to its relatively low loss, large inductance, and small capacitance. The internal modes of the fluxonium circuit identify a qubit mode, where the computational states reside, and several additional “parasitic” modes, from the charge islands in the junction array [15].

Typically, fluxonium qubit measurements are performed by dispersively coupling the circuit to a readout mode [5]. Dispersive readout, commonly used for its fast, single-shot capabilities, offers large signal-to-noise ratios and is expected to be quantum non demolition (QND) [16]. However, the fidelity and speed of this readout strategy has been limited by spurious transitions of the computational states to higher energy states [17–22], often called Measurement-Induced State Transitions (MIST). Unlike the weakly anharmonic transmon, a fluxonium circuit is highly nonlinear [3], which increases the likelihood of MIST effects [23]. Additionally, any spurious modes, such as the JJA modes mentioned previously, box modes from chip packaging, or slot line modes in the chip geome-

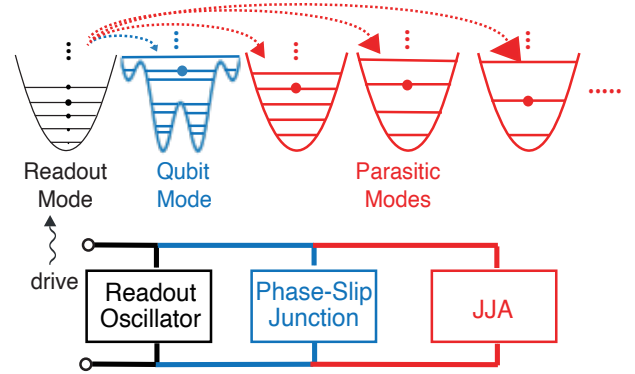


FIG. 1. Schematic of qubit state transitions driven by a readout resonator with parasitic modes from a Josephson junction array (JJA). The cartoon circuit diagram is paired with energy profiles, showing photon energy splitting into JJA parasitic modes (red), leaving enough for qubit excitation (blue).

try, may also play a role in MIST, as shown in Fig. 1. However, a detailed analysis of MIST in the presence of such spurious modes during dispersive readout of a superconducting qubit is still pending.

In this work, we analyze the state transitions during the dispersive readout of a fluxonium circuit, especially focusing on the effects that arise due to the parasitic modes of the JJA-fluxonium. Fig. 2 shows our measurement circuit for a heavy fluxonium circuit at the flux sweet spot ($\varphi_{ext} = 0.5\Phi_0$), an experimentally-relevant choice for maximizing qubit coherence [2, 5, 24, 25]; however, parasitic effects in the case of several circuit modifications are also discussed. We study population in the first three eigenstates in the qubit mode, to include experiments with

* Corresponding email: shraddha.singh@yale.edu

† Present address: Google Quantum AI, Santa Barbara, CA

a heavy fluxonium that use the first two levels (01) for computation and the second two levels (12) for measurement [5]. With our Hamiltonian derivations inspired from [26], we find that the coupling strength between the qubit mode and the parasitic modes can be ~ 100 MHz, approximately ten-fold higher than the qubit-readout coupling strength.

Treating the readout mode classically [20, 21], we perform a Floquet simulation of this system and identify predominant MIST effects, shown in Fig. 3. In particular, our simulation of the dispersive readout process identifies state transitions of the fluxonium mode under dispersive readout, which occur only in the presence of the coupling between the qubit mode and the parasitic mode. We term these phenomena parasitic-mode-assisted MIST (p-MIST). At particular readout resonator frequencies, we find that the onset of p-MIST can occur with only ~ 10 photons in the readout resonator, well within the desired power for high signal-to-noise ratios in dispersive readout [27].

Our work identifies transition pathways not seen in previous Transmon-based MIST analyses, which occur because of the highly nonlinear nature of the fluxonium spectrum. To understand the Floquet simulation results, we identify the processes that cause these transitions in Table. III using energy-conservation processes which are supported by a perturbative estimation from Fermi's Golden rule calculations. The total number of MIST effects increase by 50% in the presence of the parasitic mode with the strongest coupling to the qubit mode. Examples of some interesting MIST effects are as follows. A higher energy fluxonium state ($|2\rangle$) may exchange population with a lower energy state ($|0\rangle$), through excitation exchange with the readout resonator in the presence of a parasitic mode. In our simulations, we also observe that two higher fluxonium states are hybridized into an equal superposition state when the drive frequency is resonant with their transition frequency; such hybridization allows for increased p-MIST effects. We also observe transitions between parity conserving states which are impossible via a first-order process for $\varphi_{ext} = 0.5\Phi_0$.

We compute the rates of all p-MIST effects involving the $|1\rangle$ state, which is involved in both measurement and computation, to justify that the observed MIST effects can be significant. The rates are computed independently from, (1) the quasi-energy gap obtained via the Floquet simulations in Landau-Zener probability calculations, and (2) the Hamiltonian dynamics of the system. We ramped up the drive towards the steady-state readout mode occupation of $\bar{n}_r = 50$ to mimic dissipation in the readout resonator [20, 21]. Both methods indicate in perfect agreement that the p-MIST effects observed can be significant at a ramp-up rate of $\kappa = ??$. Additionally, we show that the residual p-MIST population in the parasitic modes, which remains after a readout pulse, begets significant dephasing of the qubit mode. Since these parasitic modes are long-lived [13] and strongly coupled to the qubit mode, such residual population must be treated with care when designing the circuit. We numerically show that the dephasing error prob-

ability due to excited parasitic modes with finite internal quality factor is above the surface code error correction threshold. This effect indicates that, without proper care, the dephasing due to p-MIST could limit the performance of a fluxonium qubit architecture.

Finally, we generalize our results to several circuit modifications by analyzing the sensitivity of the parasitic mode-qubit coupling strength for different grounding configurations, readout frequencies, parasitic mode frequencies, qubit mode frequencies, ground capacitances and number of junctions in the array. First, we show that these effects are mediated strictly by the coupling between the qubit mode and the parasitic mode. We also explore lower readout frequencies and show that increased p-MIST effects can be introduced if the parasitic frequency is an integer multiple of the drive frequency in Fig. 9. We also simulated a ~ 300 MHz circuit with larger parasitic mode frequencies, inspired by the experiment in Ref. [6]. We find that for comparable frequencies and coupling strengths this circuit has much lower number of MIST, and even in this case half the transitions are p-MIST. While our analysis does not demonstrate an exhaustive study over the entire parameter space, it shows that the parasitic modes of a junction array introduce additional constraints on circuit design of high-coherence fluxonium qubits.

The article is structured as follows: Sec. II details the readout circuit and its strong parasitic coupling under a linear JJA approximation. Sec. III covers readout dynamics, including MIST effects and dephasing from parasitic modes. Sec. IV analyzes coupling trends between parasitic, qubit, and readout modes across various circuit modifications. Finally, in Sec. V we discuss future readout strategies not covered in this analysis.

II. FLUXONIUM READOUT CIRCUIT

N	φ_{ext}	E_{J_p}	E_{C_p}	E_C	E_{C_j}	E_{J_j}	$E_{C_{q,j}}$	$E_{C_{q,p}}$	E_c
122	$0.5\Phi_0$	7.30	0.74	1.34	0.74	60	194	1.94	19.40

TABLE I. Circuit Parameters for the readout circuit in Fig. 2(a). All energies are given in GHz. Here $\Phi_0 = h/2e$ denotes the magnetic flux quantum. The capacitive energies $\frac{19.4}{C(fF)}$ GHz are computed from the corresponding capacitances C . The variables from left to right are, the number of junctions in JJA, phase-slip junction energy, phase-slip capacitive energy, differential capacitance, JJA junction energy, JJA capacitive energy, ground capacitive energy in JJA, ground capacitive energy between JJA and phase-slip junction and coupling capacitive energy. See Table IV in App. C for values of capacitances.

We consider a JJA-fluxonium circuit dispersively coupled to a readout mode as shown in Fig. 2. The parameters for circuit design used in our work, listed in Table II, are motivated by recent experiments [5, 7]. We focus on the fluxonium “sweet spot” at $\varphi_e = \pi$ for maximal qubit coherence times, and to immediately reduce the number of allowed transitions in the cir-

Qubit Readout Parameters	$\omega_{01}/2\pi$	$\omega_{12}/2\pi$	\tilde{E}_c^ϕ	$g_{\phi r}/2\pi$	$\chi_{\phi r}(01)/2\pi$	$\chi_{\phi r}(12)/2\pi$	$\omega_r/2\pi$	$\kappa_r/2\pi$
-	30 MHz	6.044 GHz	0.92 GHz	25.5 MHz	0.18 MHz	0.98 MHz	8.5 GHz	1 MHz
Parasitic-Mode Parameters	$\delta\omega_{01,\mu}/2\pi$	$\delta\omega_{12,\mu}/2\pi$	$g_{\phi\mu}/2\pi$	$g_{\mu r}/2\pi$	$\chi_{\phi\mu}(01)/2\pi$	$\chi_{\phi\mu}(12)/2\pi$	$\omega_\mu/2\pi$	\bar{n}_μ
($\mu = 2$)	0.4 MHz	14 MHz	157 MHz	4.223 MHz	-1.1 MHz	5 MHz	12.063 GHz	$6.3e-8$

TABLE II. Qubit readout and closest even mode parasitic mode ($\mu = 2$) parameters. Qubit readout parameters from left to right are: (ω_{01}) fluxon/qubit frequency, (ω_{12}) plasma frequency, (\tilde{E}_c^ϕ) qubit charging energy, ($g_{\phi r}$) qubit-readout coupling, ($\chi_{\phi r}(ij)$) dispersive shift due to parasitic modes in the two-level ij system, (ω_r) readout mode frequency, (κ_r) decay rate and corrections for parasitic modes. These quantities are derived and computed analytically. Key parameters for even parasitic modes ω_μ (mode frequency), $\delta\omega_{01,\mu}$ (fluxon frequency correction), $\delta\omega_{12,\mu}$ (plasmon frequency correction), $g_{\phi\mu}$ (qubit-parasitic coupling), $g_{\mu r}$ parasitic-readout coupling, $\chi_{\phi\mu}(ij)$ dispersive shift due to parasitic modes in the two-level ij system, and (\bar{n}_μ) thermal population at 20 mK.

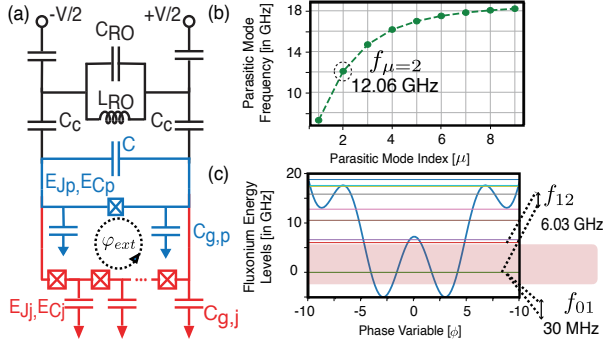


FIG. 2. (a) Fluxonium Readout Circuit. The readout oscillator (RO) in black, the phase-slip junction which decides the properties of the qubit in blue, and the Josephson junction array in red are connected in parallel. The circuit shows parasitic ground capacitances in JJA ($C_{g,i}$) and next to phase-slip junction ($C_{g,p}$), coupling capacitances (C_c), parameters for readout resonator frequency ($\omega_r/2\pi = 1/\sqrt{L_{RO}C_{RO}}$). The phase-slip junction capacitance is adjusted with an extra parallel capacitance C . V denotes drive strength. (b) Parasitic mode ω_μ frequencies. The closest even mode $\mu = 2$ has the strongest coupling to the qubit (see Fig. 19). (c) Fluxonium mode ϕ energy levels, with the highlighted area showing the first four levels for readout schemes [5].

cuit, i.e., transitions between parity-conserving states are forbidden. Here, the qubit ($\omega_{01}/2\pi$) frequency is ~ 30 MHz and the plasmon ($\omega_{12}/2\pi$) frequency is ~ 6 GHz, in this “heavy” fluxonium regime (see Table II for a full list of circuit parameters). The dispersive shift on the qubit computational states due to the readout resonator is not sufficiently strong for high signal-to-noise, at $\chi_{01} \sim 0.2$ MHz; in practice, higher excited states of the fluxonium qubit mode may be populated for improved readout fidelity [5]. Thus, to capture effects from measurement schemes that use higher levels (1, 2), we consider the population in the lowest three states of the qubit mode.

Our work specifically investigates the role of the JJA, which comprises the inductive shunt of the fluxonium. The array comprises $N + 1$ junctions and N ground capacitances due to the JJA ($C_{g,i}$) [25]. We assume an ordered array with identical junctions and parasitic ground capacitances between these junctions ($C_{g_1} = \dots = C_{g_{N-1}} = C_{g,j}$). Two additional ground capacitances near the phase-slip junction may have

different values, with $C_{g_0} = C_{g_N} = C_{g,p} \neq C_{g,i}$. The JJA fluxonium circuit has N internal degrees of freedom [15, 26]: $N - 1$ parasitic modes (μ) and one qubit mode (ϕ). Here, μ ranges between $1, \dots, N$ where the mode at $\mu = 0$ is the qubit mode ϕ . These modes are coupled via the ground capacitances. In our notation, we label the readout mode as r . The qubit charge and flux quadratures are denoted by \hat{N}_ϕ and $\hat{\phi}$ where $[\hat{\phi}, \hat{N}_\phi] = \frac{i\hbar}{2}$. We denote the photon loss and gain operators using \hat{a}_r, \hat{a}_μ and $\hat{a}_r^\dagger, \hat{a}_\mu^\dagger$, respectively. We simplify the problem by treating all but the qubit mode as harmonic oscillators as assumed in previous works [15, 21, 26]. We derive the circuit Lagrangian and Hamiltonian (see App. D). In units of $\hbar = 1$, the Hamiltonian of an undriven fluxonium measurement circuit has the form

$$\hat{H} = \hat{H}_\phi + \hat{H}_\mu + \hat{H}_r + \hat{H}_{int}, \quad (1)$$

where the qubit Hamiltonian \hat{H}_ϕ (with JJA inductive energy $E_L = E_{J_j}/N$) is

$$\hat{H}_\phi/2\pi = 4\tilde{E}_c^\phi \hat{N}_\phi^2 + E_{J_p} \cos \hat{\phi} + E_L \hat{\phi}^2/2, \quad (2)$$

the junction array and readout Hamiltonians are $\hat{H}_\mu = \sum_\mu \omega_\mu \hat{a}_\mu^\dagger \hat{a}_\mu$ and $\hat{H}_r = \omega_r \hat{a}_r^\dagger \hat{a}_r$, respectively. The qubit charging energy deviates from the target value of $E_c^\phi = 1$ GHz due to parasitic capacitance. The coupling between the three modes is described by the interaction Hamiltonian

$$\begin{aligned} \hat{H}_{int} = & g_{\phi r} \frac{\hat{N}_\phi}{N_{\phi,ZPF}} (\hat{a}_r - \hat{a}_r^\dagger) \\ & - \sum_\mu g_{\phi\mu} \frac{\hat{N}_\phi}{N_{\phi,ZPF}} (\hat{a}_\mu - \hat{a}_\mu^\dagger) \\ & - \sum_\mu g_{\mu r} (\hat{a}_r - \hat{a}_r^\dagger) (\hat{a}_\mu - \hat{a}_\mu^\dagger). \end{aligned} \quad (3)$$

where the zero-point fluctuation value is $N_{\phi,ZPF} = 1.4$.

We find that the lowest-frequency even parasitic mode $\mu = 2$ has the strongest coupling to the qubit mode (see Fig. 19 in App. C); parasitic parameters are quoted in Table II. Ref. [26] shows that the symmetry of the parallel circuit in Fig. 2 prevents coupling between odd parasitic modes (including $\mu = 1$)

and other circuit modes. We extend this result to two additional circuits, with different ground circuit configurations, showing qualitatively consistent conclusions across all in App. D. The circuits yield the same Hamiltonian when the differential capacitance C and coupling capacitance C_c are altered such that qubit frequency and qubit-readout coupling are same across all three circuits. Thus, in the rest of this work, we will use parameters of parallel circuit (see Table II) in Eq. 1 with only consider a three modes, the qubit (ϕ), the lowest parasitic mode ($\mu = 2$) and the readout resonator (r).

As reported in Table II, the qubit couples roughly six times more strongly to the parasitic mode at $\mu = 2$ than it does to the readout r . (In fact, there are four parasitic modes with coupling strengths within a factor of 10 of $g_{\phi r}$). This strong coupling indirectly couples the readout with the parasitic modes, through the qubit mode, with strength ($g_{\mu r} \propto g_{\phi \mu}$). As we show below, Such strong couplings can lead to measurement-induced state transitions assisted by parasitic modes, termed “p-MIST”. Our coupling strengths follow the same relative behaviour as observed in Ref. [26], but with a different set of parameters as chosen here. For details on other modes and their circuit parameters, see Apps. C and D.

III. PARASITIC-MODE-ASSISTED MIST: P-MIST

In this section, we analyze how the presence of a parasitic mode ($\mu = 2$) affects the dynamics of a driven fluxonium circuit in a readout context. To simulate the linear drive on the readout resonator, we add a drive term $V_d = i\xi(\hat{a}_r - \hat{a}_r^\dagger) \cos \omega_d t$ to the system Hamiltonian in Eq. 1. If we consider the fluxonium qubit mode, parasitic modes, and readout resonator, numerical analyses of several excitations in the circuit would require a prohibitively large Hilbert space. For example, the highly nonlinear nature of the fluxonium qubit spectrum results in a minimum Hilbert space dimension of at least ~ 20 for an accuracy of XXX, while we expect to drive many photons in the readout cavity. To truncate our Hilbert space to feasible dimensions for our simulations, here we only include a single parasitic mode $\mu = 2$ (as previously justified in Sec. II), and we replace the readout mode with a classical drive term [18, 20, 21] using the derivation in App. A. Under this semi-classical approximation, we the Hamiltonian of only two modes (ϕ and $\mu = 2$): $\hat{H}_{s.c.}(\bar{n}_r) = \hat{H}_0 + \hat{V}_{s.c.}(\bar{n}_r)$ which includes the parent Hamiltonian,

$$H_0 = \hat{H}_\phi + \hat{H}_\mu - \frac{g_{\phi\mu}}{N_{\phi,ZPF}} \hat{N}_\phi (\hat{a}_\mu - \hat{a}_\mu^\dagger) \quad (4)$$

and the modified drive term $V_{s.c.}$,

$$\hat{V}_{s.c.}(\bar{n}_r) = \frac{\xi_{\phi r}(\bar{n}_r)}{N_{ZPF,\phi}} \hat{N}_\phi \cos \omega_d t + \xi_{\mu r}(\bar{n}_r) \hat{N}_\mu \cos \omega_d t, \quad (5)$$

where $\xi_{\mu(\phi)r}(\bar{n}_r) = 2g_{\mu(\phi)r}\sqrt{\bar{n}_r}$ and \bar{n}_r denote the average readout photons.

Our primary task is to analyze p-MIST effects which introduce simultaneous transitions in the parasitic mode and the qubit mode. To identify the state transitions in the driven circuit, we first examine the eigenspace of H_0 . Commonly, for the analysis of a fluxonium circuit, the basis $|k\rangle_\phi \otimes |n\rangle_\mu$ is used, where the parasitic mode μ is mostly ignored [23]. We label the hybridized eigenstates of H_0 as $|\tilde{k}, \tilde{n}\rangle$ to indicate their overlap with the disjoint Hilbert space eigenstates $|k\rangle_\phi \otimes |n\rangle_\mu$.

Next, we perform a Floquet simulation of the driven circuit to identify the state transitions in the system. We simulate the system dynamics for a range of readout resonator frequencies, ω_d , and drive strengths, ξ , to identify the onset of p-MIST effects. We find that the presence of the parasitic mode $\mu = 2$ significantly increases the number of MIST effects in the system. In particular, we observe that the qubit mode can exchange population with the parasitic mode, leading to simultaneous transitions in both modes. We term these effects parasitic-mode-assisted MIST (p-MIST). In the next section, we analyze the processes that cause these transitions and quantify the rates of these effects. We use perturbative approaches and Landau Zener predictions to compute transition probabilities. Finally, we show additional simulations to demonstrate the effects of p-MIST on the qubit dephasing.

A. Floquet Simulations

Our first numerical analysis is a Floquet simulation of the Hamiltonian $H_{s.c.}$, including the qubit mode (ϕ) and the closest even parasitic mode $\mu = 2$. For the simulations, we only focus on MIST effects involving 20 levels in the Fluxonium subspace ϕ and 3 levels in the harmonic oscillator mode $\mu = 2$. In App. A we discuss the truncation used to obtain our results. We will study transitions from $|i\rangle = |0_\phi, 0_{\mu=2}\rangle, |1_\phi, 0_{\mu=2}\rangle, |2_\phi, 0_{\mu=2}\rangle, |3_\phi, 0_{\mu=2}\rangle$. The analysis in this section, which can be replicated for any other parasitic mode, will consider the regime of negative detuning where, $\omega_{\mu=2} > \omega_d = \omega_r \gg \omega_q$.

Inspired by [20, 21], we extract p-MIST effects through branch analysis of fluxonium eigenstates in a Floquet simulation. The simulation begins in an eigenstate $|n\rangle$ of the circuit Hamiltonian \hat{H}_0 . Next, we compute the eigenstates of the modified Hamiltonian $\hat{H}_{s.c.}$ with $\bar{n}_r = 1$ at $t = 0$, corresponding to a single photon increase in the readout resonator, i.e., $|\tilde{i}, \tilde{0}\rangle_{\bar{n}_r=1}$. We then identify the eigenstate $|m\rangle$ of \hat{H}_0 that has maximum overlap with $|n\rangle$, identifying it as the eigenstate associated with $|m\rangle$ from the previous time step. This process is repeated with the increment $\Delta\bar{n}_r = 1$ at $t = 0$, such that at each time step t_k , a new state is chosen from the Floquet eigenspace of the modified Hamiltonian as,

$$|m_{\bar{n}_r=k}\rangle : \max_{m'} |\langle m_{\bar{n}_r=k-1} | m'_{\bar{n}_r=k} \rangle|^2. \quad (6)$$

Our method is different from Ref. [20, 21] in that we perform the branch analysis of the modified Hamilto-

S.No.	MIST	Drive Frequency (ω_d)	p-MIST	Process (see App. A 3 and Fig. ??)
1.	$ \tilde{0}, \tilde{0}\rangle \xleftarrow{\bar{n}_r=13} \tilde{13}, \tilde{0}\rangle$	8.64 GHz	×	(3r)
2.	$ \tilde{0}, \tilde{0}\rangle \xleftarrow{\bar{n}_r=48} \tilde{4}, \tilde{2}\rangle^*$	8.71 GHz	✓	(2r)→(4r)
3.	$ \tilde{0}, \tilde{0}\rangle \xleftarrow{\bar{n}_r \rightarrow 0} \tilde{8}, \tilde{0}\rangle$	8.84 GHz	×	(2r)
4.	$ \tilde{0}, \tilde{0}\rangle \xleftarrow{n_r=26} \tilde{6}, \tilde{1}\rangle^*$	9.25 GHz	✓	(2r)→(1r)
5.	$ \tilde{0}, \tilde{0}\rangle \xleftarrow{n_r=48} \tilde{6}, \tilde{1}\rangle^*$	9.28 GHz	✓	(2r)→(1r)
6.	$ \tilde{0}, \tilde{0}\rangle \xleftarrow{\bar{n}_r=12} \tilde{3}, \tilde{1}\rangle$	9.36 GHz	✓	(2r)
7.	$ \tilde{1}, \tilde{0}\rangle \xleftarrow{\bar{n}_r=32} \tilde{17}, \tilde{0}\rangle$	8.56 GHz	×	(4r)
8.	$ \tilde{1}, \tilde{0}\rangle \xleftarrow{\bar{n}_r=4} \tilde{7}, \tilde{0}\rangle$	8.73 GHz	×	(2r)
9.	$ \tilde{1}, \tilde{0}\rangle \xleftarrow{\bar{n}_r=19} \tilde{12}, \tilde{1}\rangle$	9.02 GHz	✓	(4r)
10.	$ \tilde{1}, \tilde{0}\rangle \xleftarrow{\bar{n}_r=13} \tilde{2}, \tilde{1}\rangle$	9.05 GHz	✓	(2r)
11.	$ \tilde{1}, \tilde{0}\rangle \xleftarrow{\bar{n}_r=8} \tilde{14}, \tilde{0}\rangle$	9.31 GHz	×	(3r)
12.	$ \tilde{1}, \tilde{0}\rangle \xleftarrow{\bar{n}_r=3} \tilde{9}, \tilde{0}\rangle$	9.41 GHz	×	(2r)
13.	$ \tilde{2}, \tilde{0}\rangle \xleftarrow{\bar{n}_r=2} \tilde{12}, \tilde{0}\rangle$	9.00 GHz	×	(2r)
14.	$ \tilde{2}, \tilde{0}\rangle \xleftarrow{\bar{n}_r=37} \tilde{0}, \tilde{2}\rangle$	9.06 GHz	✓	(2r)
15.	$ \tilde{2}, \tilde{0}\rangle \xleftarrow{\bar{n}_r=13} \tilde{5}, \tilde{1}\rangle^*$	9.41 GHz	✓	(1r)→(2r)

TABLE III. Measurement-induced-state-transitions observed in Fig. 3. Column 1 lists the MIST effects that start at the lowest average readout photon number \bar{n}_r . In some cases, the label $\bar{n}_r \rightarrow 0$ indicates that the drive frequency is exactly resonant with the transition frequency. The asterisk ‘*’ indicates a hybridized state due to preceding transitions^a. Column 2 represents the drive frequency ω_d at which these transitions occur. Column 3 indicates if the process cannot occur without the parasitic mode, denoted as p-MIST. Column 4 indicates the number of readout photons (#r) involved in the energy-conserving process which is responsible for these transitions. We give Fermi’s golden rule rates calculated up to second-order terms for these processes in App. A 3.

^a $|\tilde{4}, \tilde{2}\rangle^* : |\tilde{4}, \tilde{2}\rangle \xleftarrow{\bar{n}_r=5} |\tilde{14}, \tilde{2}\rangle$ at $\omega_d = 8.71$ GHz
 $|\tilde{6}, \tilde{1}\rangle^* : |\tilde{6}, \tilde{1}\rangle \xleftarrow{\bar{n}_r \rightarrow 0} |\tilde{3}, \tilde{1}\rangle$ at $\omega_d = 9.25, 9.28$ GHz
 $|\tilde{5}, \tilde{1}\rangle^* : |\tilde{5}, \tilde{1}\rangle \xleftarrow{\bar{n}_r=11} |\tilde{17}, \tilde{0}\rangle$ at $\omega_d = 9.41$ GHz

nians $H_{s.c.}(\bar{n}_r)$ at a fixed time $t = 0$. For each $|m_{\bar{n}_r=i}\rangle$ tracked in the branch, we compute:

1. the expectation values of $\hat{n}_t = \sum_i i |i_t\rangle \langle i_t|$ where i_t are the bare fluxonium eigenstates,
2. the expectation value of $\hat{n}_\mu = a_\mu^\dagger a_\mu$, i.e., the number operator of the harmonic oscillator defined by the parasitic mode, and
3. the quasi-energy spectrum $\epsilon_i \bmod \omega_d$.

Fig. 3 illustrates our main result, showing p-MIST for initial fluxonium states $|n\rangle$ of $|0\rangle$, $|1\rangle$ and $|2\rangle$. We show the fluxonium excitation (top-row) and parasitic mode excitation (bottom-row) values for the branch analysis of hybridized states $|m\rangle$ closest to the disjoint states where the fluxonium subspace is $i = 0, 1, 2$ and that parasitic modes begin in the ground state with $\bar{n}_\mu = 0$. We focus on readout drive frequencies between 8.5 – 9.5 GHz (a relatively high-frequency choice, to reduce thermal, photon shot-noise induced dephasing in the qubit compared to lower-frequency bands). The p-MIST effects occur at various values of ω_d , corresponding to simultaneous jumps in the population of the modes ϕ (Figs. 2a-2c, top row) and $\mu = 2$ (Figs. 2a-2c, bottom row), as \bar{n}_r varies. At these points, an avoided crossing in quasi-energies confirms the hybridization of the two states involved in the population exchange (Figs. 12-14).

Additional resonances may occur at alternate drive frequencies not shown in Fig. 2. Table III lists all transitions observed in our Floquet simulations,

and associated processes which cause them, identified through a perturbative analysis (see App. A 3). Here, we list our key findings.

- **p-MIST Effects:** Such effects occur only when qubit-parasitic mode coupling ($g_{\phi\mu}$) is non-zero, covering roughly half the number of transitions listed in Table. III. Such transitions will not be captured if parasitic modes are ignored in the Floquet simulations. All p-MIST effects show a simultaneous change in population in both the qubit and the parasitic mode. For example, in transition 9, the hybridized subspace shows a transition which is closest in disjoint subspace to the state transitions $|1\rangle_\phi \leftrightarrow |12\rangle_\phi$ in the fluxonium subspace and $|0\rangle_{\mu=2} \leftrightarrow |1\rangle_{\mu=2}$ in the parasitic mode subspace. Another interesting instance is 15, where if the parasitic mode was absent the transition $|\tilde{17}, 0\rangle \leftrightarrow |\tilde{2}, 0\rangle$ is a 3 readout photon process, however, in the presence of parasitic mode $\mu = 2$ this process is broken down to be mediated in the hybridized states by $|\tilde{5}, \tilde{1}\rangle$ via two 1 readout and 2 readout processes. The number of p-MIST effects will increase when other parasitic modes, with coupling comparable to or greater than the qubit-readout coupling ($\mu = 4, 6$), are included in the Floquet simulations. See Fig. 19 for absolute coupling strengths.
- **Downward-transition:** In transition 13, we observe downward transitions from a higher

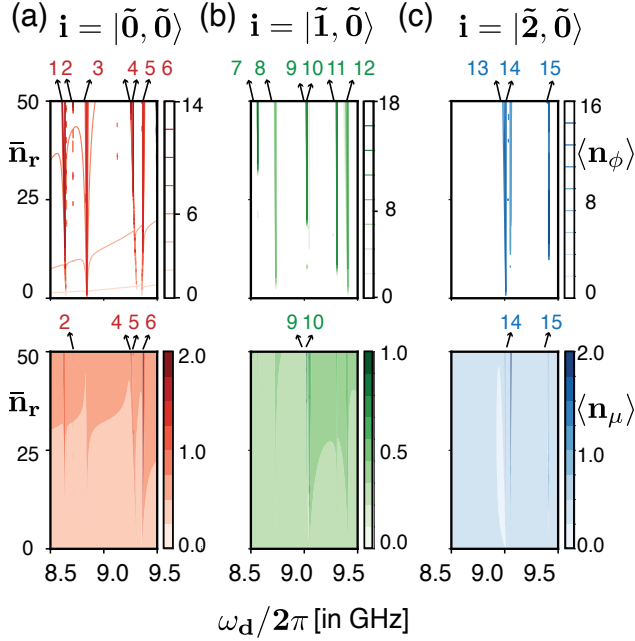


FIG. 3. p-MIST effects in Floquet Simulations. Columns show results when the initial state in the branch analysis is the dressed hybridized eigenstate $i = |\tilde{k}, \tilde{0}\rangle$, with maximum overlap with un-hybridized states $|k\rangle_\phi \otimes |0\rangle_{\mu=2}$. (Top row) Average fluxonium excitation $\langle n_\phi \rangle$. (Bottom row) Average excitation $\langle n_\mu \rangle$ of the first-even parasitic mode ($\mu = 2$). All transitions observed in this figure are explicitly listed in Table III and plotted in Figs. 12–14 of App. A3.

fluxonium level ($|2\rangle_\phi$) to a lower fluxonium level ($|0\rangle_\phi$), a process that would release transition photons instead of absorbing readout photons, in the absence of parasitic modes. This is possible because in the presence of parasitic mode, the state $|\tilde{0}, \tilde{2}\rangle$ has a higher energy compared to $|\tilde{2}, \tilde{0}\rangle$ such that absorbing two readout photons results in a p-MIST which is closest to a downward state transition in the disjoint fluxonium subspace.

- **Rabi-Flopping:** In transitions 3–5 we observe Rabi Flopping between two states upon addition of a single photon, such that, the states hybridize into an equal superposition of the two states involved. For example, in transitions 4, 5, levels $|3\rangle_\phi$ and $|6\rangle_\phi$ converge to a population of $\langle n_\phi \rangle = 4.5$ in the fluxonium subspace at $\bar{n}_\mu \rightarrow 0$ (see Fig. 12 in App. A3). While this effect is not limited to p-MIST, we highlight the presence of these effects as an accelerator to p-MIST effects since at each transition frequency ω_{ij} in the fluxonium subspace there are several possible transitions $|\tilde{i}, \tilde{n}_\mu\rangle \rightarrow |\tilde{j}, \tilde{n}_\mu\rangle$ for all \tilde{n}_μ . A result of this effect is that a parasitic process $|\tilde{6}, \tilde{1}\rangle \leftrightarrow |\tilde{0}, \tilde{0}\rangle$ which is a 5 readout-photons process will now only require 2 readout photons, thus increasing the chances of an avoided crossing.

We note that certain MIST effects, p-MIST or not, involve the unexpected transitions at the flux sweet

spot [28] between parity-conserving states, due to virtual excitations via non-parity-conserving states.

Our findings reveal that neglecting parasitic modes can result in incorrect predictions of MIST-free frequency ranges. Having identified key transitions in the target readout range, we will now calculate their transition probabilities to assess the impact on readout fidelity.

B. Transition Probability

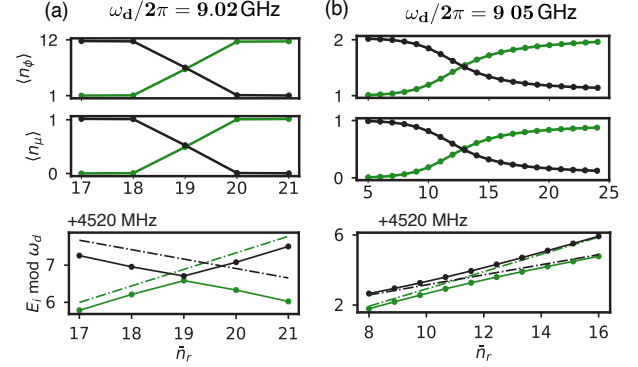


FIG. 4. Examples of p-MIST using transitions 6 (a) and 7 (b) from Table III involving the $|\tilde{1}, \tilde{0}\rangle$ state. (Top row) Fluxonium subspace $\langle n_\phi \rangle$. (Middle) Parasitic mode subspace $\langle n_\mu \rangle$. (Bottom) Stark-shifted eigen-energies (dashed) and quasi-energies (solid) from Floquet simulations, corresponding to the initial state i as per the legend. Inset shows avoided crossing of quasi-energies. Floquet results are extracted from numerical data used for Fig. 3.

In this section, we estimate the quasienergies and rates of exemplary p-MIST transitions, using perturbation theory and the Landau-Zener formalism, respectively. In both the Floquet simulations and Landau-Zener approximations, the spectral gap of an associated transition is a critical figure-of-merit in determining the diabatic energy exchange probability. Here, the avoided crossing of states $|\tilde{1}, \tilde{0}\rangle$ and XXXX [5] is shown in Fig. 4. The simultaneous exchange of population in the qubit mode ϕ , shown in Fig. 4(a), and the parasitic mode $\mu = 2$, shown in Fig. 4(b), confirms that the transitions are indeed p-MIST. Here, Fig. 4(c) shows the avoided crossing at the transition point.

For small drive amplitudes compared to the gaps in the spectrum, a simple estimate of the eigenenergies using perturbation theory is possible (see A2). Fig. 3 shows the eigenenergies calculated by estimating the Stark shift from the readout drive onto each state (dotted lines). Comparing our estimates to the numerically obtained energy gaps in the quasi-energies (solid lines), we find agreement within XXX. The remaining disagreement between the quasi-energies and the estimated eigenenergies suggests that higher-order or non-perturbative corrections become relevant at the sub-XXX% level. Notably, both the transitions shown in Fig. 4 occur at low average number of readout photons of $\bar{n}_r = 12, 19$, well within the power typically needed for high signal-to-noise dispersive read-

out of superconducting qubits [ER: get citation from earlier].

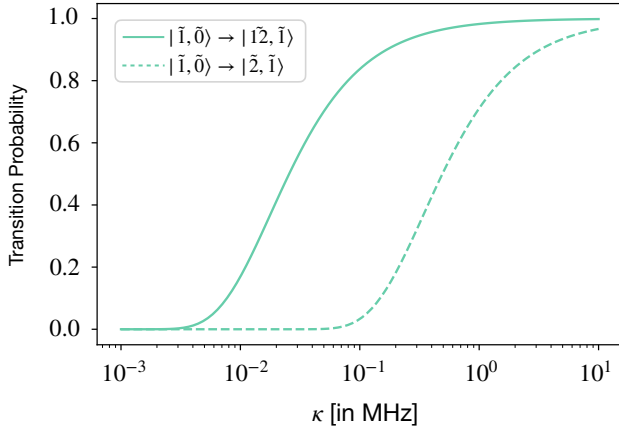


FIG. 5. Landau-Zener probability against the parameter κ which determines the change in drive strength $\xi_{\mu/\phi} = 2g_{\mu/\phi}\sqrt{\bar{n}_r(t)}$ where $n_r(t)$ follows Eq. 7. [SS: Yet to add unitary evolution curves]

Next, we use the gaps in the quasi-energies to compute the Landau-Zener (LZ) probabilities, using the method described in Ref. [29]. For this analysis, we assume a time dependence of the average readout photon number of

$$\bar{n}_r(t) : \bar{n}_r(1 - e^{-\kappa_r t/2})^2, \quad (7)$$

which includes a ring-up time of $1/\kappa$, according to the readout resonator bandwidth [19–21]. Note that the time interval is again given by $\Delta\bar{n}_r = 1$, thus replicating our previous model used for Floquet simulations with $\bar{n}_r = 50$. As expected, varying κ changes the probability of transitions, plotted in Fig. 5 (for details see App. A 4). [ER: we have a different $\bar{n}_r(t)$ dependence though no?] We compare these LZ transition probabilities to the overlap of the initial state evolved under the unitary $U = e^{i\hat{H}_{s.c.}t}$ with the Floquet branch state at $t_f = \frac{10}{\kappa_r}$: $|\langle m_{\bar{n}_r=n_f} | \mathcal{U}(t_f) | i \rangle|^2$. Unlike Ref. [21] we do not find perfect agreement in these two cases due to Landau-Zener-Stuckelberg transitions..? This indicates that the two-state physics captured by Landau-Zener transitions may not be correct to study strengths of fluxonium transitions.

C. Qubit Dephasing post-Readout

Here, we consider implications of p-MIST *after* the readout pulse is executed, in the context of a larger quantum circuit where the fluxonium mode is used as a qubit. In general, the parasitic modes are long-lived, with internal quality factors of $\sim 10^4$ [13, 30]. Spurious excited state population of the parasitic mode introduced by p-MIST during readout can introduce correlated dephasing of the qubit, through the large dispersive interaction $\chi_{\mu\phi} \sim 1$ MHz (see Table II). If the parasitic mode is excited, the qubit accumulates a phase at a constant rate $\chi_{\mu\phi}\bar{n}_\mu$, in the absence of any decay. However, for finite internal quality factor Q_μ ,

the parasitic mode decays at a rate $\kappa_\mu = Q_\mu/\omega_\mu$. In this scenario, the qubit dephasing is not deterministic but a Poissonian process which relies on the random decay of the parasitic mode.

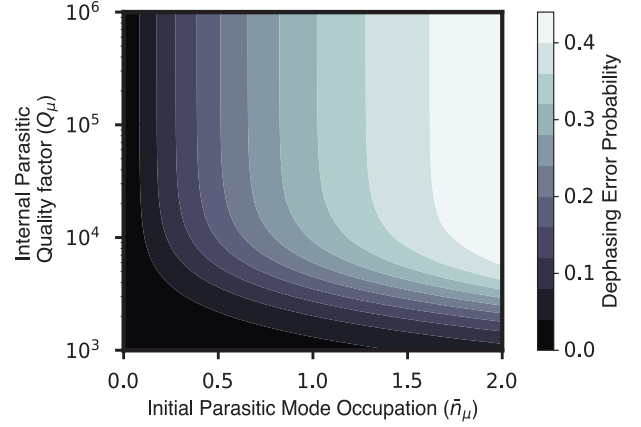


FIG. 6. Dephasing error probability due to random decay of an excited parasitic mode after p-MIST at finite Q_μ .

We performed a master equation simulation of dephasing of a qubit state $|+\rangle$ under the Hamiltonian $H = \chi_{\phi\mu}\hat{a}_\mu^\dagger\hat{a}_\mu\sigma_z$ and dissipation under $\sqrt{\kappa_\mu}\hat{a}_\mu$ when the initial parasitic mode population is \bar{n}_μ . We plot in Fig. 15 the infidelity of the state after the parasitic mode reaches a steady state at $T_f = 10/\kappa_\mu$ for various Q_μ and \bar{n}_μ . Specifically, we find that for internal quality factors of the parasitic mode Q_μ of 10^4 about XXX population in the parasitic mode is needed to introduce a dephasing error probability of 0.01, already past the threshold of surface code decoders [31]. Given that the population of the parasitic modes is about $\bar{n}_\mu \sim 1$ at a readout power of ~ 10 photons, we expect that qubit coherence can be limited by p-MIST in circuit designs which do not anticipate them.

Thus, with various methods used in these analyses we have quantitatively demonstrated that p-MIST effects restrict the frequency landscape available for high-fidelity readout of a fluxonium qubit. We have confirmed that dephasing due to the drive and thermal effects is negligible (see Apps. A 5 and C). In the next section, we will analyze the range of various mode frequencies responsible for these effects.

IV. EFFECTS OF CIRCUIT MODIFICATIONS ON P-MIST

The p-MIST effects shown in the previous section can be mitigated in various ways, by adjusting the qubit frequency, readout resonator frequency, and parasitic mode frequencies, as well as reducing parasitic mode and qubit coupling strengths. In this section, we explore the impact of each of these components individually. All equations analyzed in this section were derived in Ref. [26] for the circuit in Fig. 2, and we have extended these results to circuits with different grounding configurations in App. D.

captured in transition 15 of Table II. To emphasize the correctness of these predictions we zoom into the transitions captured from Floquet simulations (see Sec. III) in Fig. 8. The labels correspond to the disjoint subspaces for clarification but the energy conservation uses the eigen-energies of the hybridized state for H_0 in Eq. 5. A positive # denotes emission while a negative denotes absorption. For example, in transition 2 emits 3 readout photons which is converted into 2 parasitic mode photons absorbed by the mode $\mu = 2$ and the transition $|0\rangle_\phi \leftrightarrow |4\rangle_\phi$ in the fluxonium subspace. This equation gives us the following intuition which we verify for different ranges of mode frequencies

a. Drive Frequency: According to Eq. 9, the drive frequency ω_d should be chosen such that it is far from the parasitic mode frequencies. If $\omega_d \gg \omega_\mu$, a single readout photon will cause excitations in modes with higher frequency. Given that the first three modes couple to the qubit more strongly than the readout, we need to be above these modes. However, this readout frequency range is unreasonable and does not give full guarantee of absence of MIST effects completely from parasitic modes with lower coupling. On the other hand, if we reduce the readout frequency we see an increased number p-MIST effects in Fig. 9. This range of drive frequency includes the frequency which is half of the parasitic mode and hence constitutes a very busy p-MIST profile. Further reducing drive frequency can cause issues related thermal population.

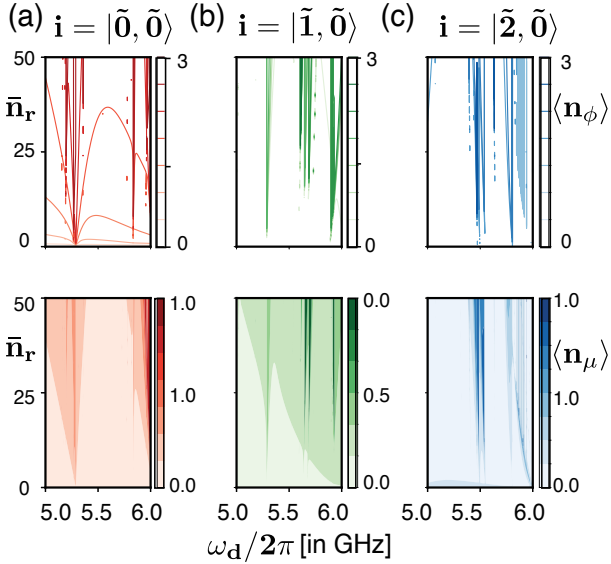


FIG. 9. Floquet simulations at lower readout frequencies.

b. Parasitic Mode Frequency: Another approach towards mitigating p-MIST effects is to adjust ω_μ so that $\omega_r \ll \omega_\mu$ for $\mu = 2$, potentially improving the circuit. This is feasible with granular-aluminum (GrAl) inductive shunts, though they are lossy [27]. Recent efforts are applied towards improving GrAl shunts.

For the JJA parameters, to provide some quantitative arguments in this direction we discuss the dependency of ω_μ for even parasitic modes (e) on various

circuit variables.

$$\frac{\omega_\mu^e}{2\pi} = \sqrt{8E_{c,\mu}^e E_{J_j}}, \quad \text{where} \quad (10)$$

$$E_{c,\mu}^e = \left[\frac{1}{E_{C_j}} + \frac{1}{4E_{g_j}s_\mu^2} \right]^{-1}. \quad (11)$$

Here, $s_\mu = \sin(\frac{\pi\mu}{2(N-1)})$. Here, $E_{c,\mu}^e$ is the charging energy of an even parasitic mode. All other variables used are defined in Table II. The second term increases quadratically with μ , causing a quadratic decrease in frequency for smaller μ . For parasitic modes with strong coupling, $\mu \ll N$, for large N , the charging energy is $\tilde{E}_{c,\mu}^e = 4E_{g_j}s_\mu^2$, which is inversely proportional to N^2 and directly proportional to E_{g_j} . Larger N and parasitic ground capacitance C_{g_j} lead to lower frequencies for these modes, which is unfavorable. Fig. 16 in App. C shows the dependence of charging energy of parasitic modes as well as qubit modes with respect to parasitic ground capacitance. Decreasing the parasitic ground capacitance reaches the target charging energy for qubits. At the same time it also increases the parasitic mode charging energy, and thus its frequency. Thus, reducing parasitic mode frequencies in this limit involves lowering the capacitance $C_{g,i}$ (see Fig. 16), but this is constrained by practical limits of around 0.1 fF per junction due to the gap to the ground plane. The trend with respect to N is not so straightforward. Note that changing N changes the target inductance of the qubit. Keeping the same inductance as N changes requires one to increase E_{J_j} by the same factor as N . To keep the E_{J_j}/E_{C_j} ratio the same this leads to an increase in E_{C_j} , thus supporting our argument for large N even further. Decreasing N on the other hand increases nonlinearity as well as flux noise [SS: CITE].

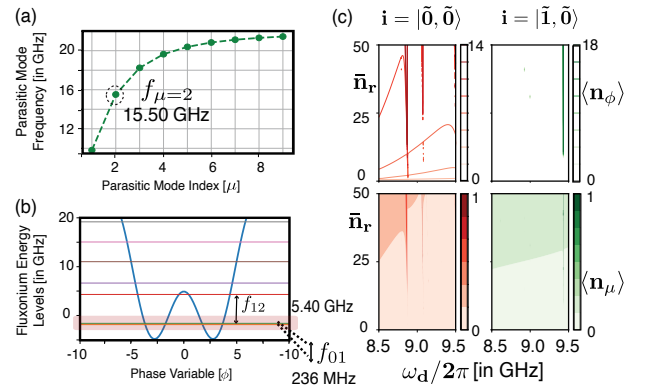


FIG. 10. MIST with a fluxonium circuit of qubit frequency ~ 300 MHz and lowest even parasitic mode frequency $\omega_{\mu=2} \sim 16$ GHz. (a) Fluxonium energy spectrum (b) Parasitic mode frequencies (c) Floquet simulations for the semi-classical Hamiltonian in Eq. 5 with the alternative circuit parameters. Considerably lower number of MIST effects due to the increased distance between the readout frequencies considered and the parasitic mode frequency.

In the previous sections we focused on ~ 30 MHz fluxonium frequency. To generalize our results to other experiments, we consider another circuit inspired by parameters in [6] and show p-MIST effects

in a 236 MHz fluxonium. The parasitic mode frequency of the $\mu = 2$ mode is $\omega_{\mu=2} = 15.51$ GHz. The coupling strengths are as follows, $g_{\phi r} = 37$ MHz, $g_{\phi\mu} = 216$ MHz, $g_{\mu r} = 6$ MHz. The plasmon frequency is $\omega_{12} = 5.4$ GHz. For these parameters, even though the coupling strengths are on par with Table II, since the parasitic mode frequency of the even mode $\mu = 2$ is larger by ~ 4 GHz, we expect fewer transitions. This has been verified in the Fig. 10. Importantly, here we only plot results for $|\tilde{0}, \tilde{0}\rangle$ and $|\tilde{1}, \tilde{0}\rangle$ because given Ref. [6] uses only the first two levels for readout as well as computation. The detailed circuit parameters are given in App. D.

Fig. 10 shows that the number of p-MIST effects is considerably lower than in this case. This is due to the increased distance between the readout frequencies considered and the parasitic mode frequency. This suggests that the choice of qubit frequency can be a crucial factor in reducing p-MIST effects. However, a detailed understanding of this Floquet profile is necessary to make proper claims in relation to reduced MIST effects, and is left as future direction. The convergence plot for this circuit is shown in App. D.

V. CONCLUSION AND FURTHER WORK

In this work, we have analyzed the impact of parasitic modes on the readout of a fluxonium qubit. This work shows that transitions in a fluxonium circuit triggered by a parasitic mode of the JJA, which we call p-MIST effects, can occur with considerable rates from coupling of the parasitic modes with the readout and qubit modes. The parallel circuit considered in this work utilizes a specific symmetry which removes the coupling between the lowest frequency mode and the qubit. We show that this symmetry is preserved if the readout resonator is coupling to a floating or grounded fluxonium at a single point. Our analysis considers fluxonium at the sweet spot which introduces additional symmetries forbidding transitions between parity-conserving states via first-order transitions. Despite these various symmetries and our modest assumption of no self-nonlinearity in the JJA or the readout, our results show that a strong coupling of parasitic modes to the qubit mode still triggers p-MIST at low average readout photons. Not only do p-MISTs lower the onset of MIST effects to ~ 10 readout photons but also significantly dephase the qubit, both of which directly limit the readout fidelity [32].

We analyze the trend in p-MIST for various drive frequencies, parasitic mode frequencies, coupling constants, and circuits with two different qubit frequencies equal to ~ 30 and ~ 300 MHz. While our work does not constitute a thorough analysis of the entire parameter space by any means, it highlights the significant impact of parasitic modes in a driven fluxonium circuit. The assumptions we make are crucial to are MIST analysis. Increasing N can reduce the nonlinearity of the parasitic modes, with insights provided in Sec. IV. We also neglect the self-nonlinearity of the readout mode which has been a common practice in recent MIST-related analysis [17, 20, 21]. While

the effects of nonlinearity in parasitic and readout modes can have significant impact on the readout fidelity, Floquet simulations including self-nonlinearity of these modes is beyond the scope of our work. Analysis of a disordered array could be an interesting extension of our work as it may lead to lower coupling between the qubit and parasitic modes. We analyze state transitions in a driven fluxonium circuit using numerical methods under the following assumptions.

To advance practical implementation and reduce fluxonium MIST in the dispersive readout, we suggest adding noise to the Floquet framework [33] and linking our results to readout fidelity values using input-output theory. Future work should also incorporate the intrinsic nonlinearity of both the junction array modes and the readout mode. Mitigating parasitic mode excitations could involve varying junction energies along the array to localize collective modes, thereby altering the parasitic mode spectrum and reducing excitation probability. Alternative readout schemes like longitudinal readout or cloaking could also be explored [34–36]. Given the strong coupling between parasitic modes and fluxonium, these modes could potentially enhance fluxonium qubit readout. We propose using a feedline with a Purcell filter to tailor the spectrum and protect the qubit, reducing capacitive loading constraints.

Our results present a first analysis toward understanding the role of parasitic modes in the readout dynamics of a fluxonium circuit. Although the circuit parameters used in this work are closest to a fluxonium circuit, these results can be generalized to other high-anharmonic superconducting circuits with similar mode frequencies.

VI. ACKNOWLEDGMENTS

We thank Akshay Koottandavida, Daniel K Weiss, Connor Hann, Kyungjoo Noh, and Simon Leiu for fruitful discussions. We are grateful to Simone Severini, Bill Vass, Oskar Painter, Fernando Brandão, Eric Chisholm, and AWS for supporting the quantum computing program.

Appendix A: Driven Fluxonium Circuit

Here, we will discuss the analyses involved for the driven fluxonium circuit including the semi-classical approximation and methods used in Sec. III to compute the readout efficiency.

1. Approximations for Numerical Modelling

We use the following three approximations to make the problem at hand simpler

- Restriction to $\mu = 2$. We restrict our analyses to the closest even parasitic mode that couples most strongly to the qubit and the readout as evident from Fig. 16(d). This assumption helps

us to lower bound the errors. Although it will be an interesting study to see if there are transitions caused due to higher modes that are more probable but in this work we aim at a proof of principle quantitative evidence of the presence of such transitions even with out modest assumptions.

- **Semi-classical drive approximation.** This approximation treats the readout resonator classically as described in Refs. [18–21] reducing one mode from our numerical simulation. This assumption is essential since unlike the case of transmon or fluxonium without collective modes, with all the above approximation, a full quantum simulation of the problem will still require three modes.
- **Linear JJA Approximation.** We assume that the parasitic modes behave as linear oscillators due to the large $E_{J_j}/E_{C_j} = 200$ ratio. This approximation is explained in App. C. The non-linear corrections to our results, while essential, is beyond the scope of this work. For details on how nonlinear corrections affect different circuit parameters in play we direct the readers to Ref. [26]. Due to this assumption, we can use a Hilbert size of 20×3 where only three levels are assumed in the linear parasitic mode subspace. In the presence of nonlinearity, the Hilbert size would need to be much larger to capture the required effects. Note that for the conclusions drawn in this paper, we are only interested in the presence of p-MIST effects and do not claim to quantify how many such transitions can be present. Hence, 3 levels in the parasitic mode are enough. In addition, we have verified that changing the truncation of the parasitic mode to 10 levels does not change the energy spacing.

2. Stark Shift

To observe a state transition the primary requirements are high charge matrix elements and low energy difference. The eigen-energies of the states in question are changed with an increase in the number of readout photons or, in this case, the drive strength. So, in this section, we compute the stark shifted eigen-energies which can help in the prediction of an avoided crossing, given \bar{n}_r, ω_r and the charge matrix elements. These stark shift formulas are used in the computing the probability of transitions using generalized Fermi's golden rule and Landau-Zener calculations. Let $|i\rangle$ be a state in the eigenspace of $H_{int} = H_\phi + H_{\mu=2} + g_{\phi\mu}\hat{N}_\phi\hat{N}_\mu$. Following derivations in App. C the ac stark-shift in the energy of state $|i\rangle$ at an average number of readout photons \bar{n}_r is given by,

$$\chi_i(\bar{n}_r) = 2\bar{n}_r \sum_f \omega_{if} \left[\frac{g_{\phi r} |\langle i|\hat{N}_\phi|f\rangle|^2}{\omega_d^2 - \omega_{if}^2} + \frac{g_{\mu r} |\langle i|\hat{N}_\mu|f\rangle|^2}{\omega_d^2 - \omega_{if}^2} \right] \quad (\text{A1})$$

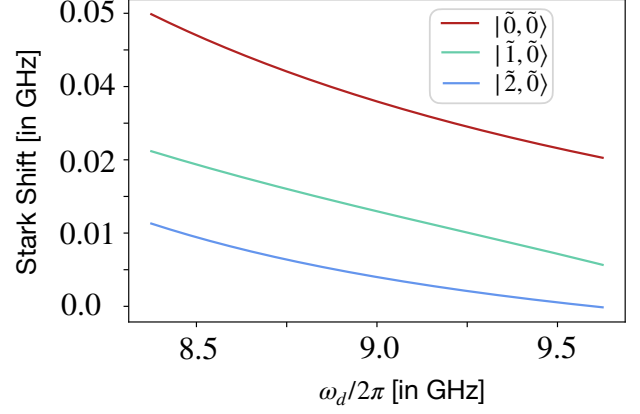


FIG. 11. Stark shift in different qubit levels under observation for readout computed using Eq. A1.

Here $\omega_{if} = E_f - E_i$ denote the energy difference in the eigen-energies of the $|i\rangle$. The impact due to the second term as expected is much smaller than the first term, and hence $g_{\phi r}$ primarily governs this stark shift.

3. Generalized Fermi's Golden Rule Rates

Below we guess process responsible for each transition using first and second order fermi's golden rule calculations. We have computed rates using fermi's golden rule up to second order terms, as many of these transitions occur between a parity-conserving states, a forbidden first order transition. We compute these transitions involving up to 4 readout photons, as suggested by energy conservation. Under the same classical approximation, we can identify our parent Hamiltonian as H_0 and perturbation V as follows,

$$H_0 = H_\phi + \omega_\mu \hat{a}_\mu^\dagger \hat{a}_\mu + g_{\phi,\mu} \hat{N}_\phi \hat{N}_\mu \quad (\text{A2})$$

$$V = 2\sqrt{\bar{n}_r} (g_{r,\phi} \hat{N}_\phi + g_{r,\mu} \hat{N}_\mu) \sin \omega_d t, \quad (\text{A3})$$

where μ is the density of states which will be a Dirac Delta function in the absence of loss while it will be Lorentzian in the presence of loss $\frac{\kappa}{2\pi} = 50$. In units of \hbar we have,

$$\Gamma_{i \rightarrow f} = |\langle f|H_1|i\rangle|^2 \mu(E_i - E_f) \quad (\text{first-order}) \quad (\text{A4})$$

$$= \sum_m \frac{|\langle f|H_1|m\rangle \langle m|H_1|i\rangle|^2}{|E_i - E_m - k\hbar\omega_d|^2} \mu(E_f - E_i - n\hbar\omega_d) \quad (\text{second-order}) \quad (\text{A5})$$

We use a Lorentzian density of states at a $\frac{\kappa}{2\pi} = 1.5$ KHz. Here $k < n$ is used to compute the detuning with the intermediate state involved in the transition. Note that increasing the width of the Lorentzian κ resulting in an increase in the FG rates. Thus, here the decay rate does not yield any insights into the diabaticity at the transition, and hence the κ variation here is not the same as the κ variation in Sec. ??.

While these calculations include stark shifts in the energies of the states, we know that the first-order perturbative correction is not enough for some of the

more higher states as seen in the comparisons of quasi-energies from Floquet simulations and predictions of stark shifted transitions. Thus, the computation below is only based on a heuristic developed from this approximate calculation. All transitions are computed at $\bar{n}_r = 50$. We note that the Fermi's golden rule calculations higher rates at the frequencies predicted by $g_{\phi\mu} = 0$ case where the two frequencies are extremely different, for example, transitions 10 and 14. This happens since the Fermi's golden rule calculations are only approximately computing the stark-shifted energies for states which are more hybridized due to the presence of coupling $g_{\phi\mu}$. This behaviour is evident in Figs. 12, 13, 14. We will compare the considerable FG rates with well-separated quasi-energy gap at the avoided crossings Δ_{ac} seen in these figures.

For the case of $|i\rangle = |\tilde{0}, \tilde{0}\rangle$ shown in Fig. 12, we quote the rates for each process and state how many readout photons were involved, guess the possible intermediate state and whether it could be a first- or second-order process. This heuristic analysis is still interesting since it helps us understand the processes involved behind general MIST processes and p-MIST processes, identifying any unique feature or extremely high rates, if so.

- 1 This is a first order transition involving three readout photons ($3r$) which yields a Fermi's golden rule rate of 40 KHz.
- 2 The first process is a second-order process which absorbs two photons ($2r$) through an intermediate state with energy close to $E_i + \omega_r$ at a rate of 4 MHz where $\Delta_{ac} = 4$ MHz. The second process is a second-order which absorbs four photons ($4r$) through an intermediate state close to $E_i + 3\omega_r$ at a rate of 22 KHz.
- 3 This is a Rabi transition involving a virtual state via a second-order two-photon process ($2r$) at a rate of 0.028 KHz.
- 4-6 The first transition is a second order two-photon process $2r$ with an FG rate of 1.26 KHz at $\omega_r = 9.36$ GHz. The second process is a Rabi transition at a rate of 10 KHz.

Next, we look at the transition rates for the $|\tilde{0}, \tilde{1}\rangle$, the state involved in the computation as well as readout in a low-frequency fluxonium, shown in Fig. 13.

- 7 This is a second order process involving four readout photons ($4r$) at a rate of 21 KHz. The intermediate state involved is close to a frequency of $E_i + 3\omega_r$.
- 8 This is a second order process involving two readout photons ($2r$) with a transition rate of 45 KHz. The energy gap at the avoided crossing for this transition is less than 1 MHz.
- 9 This is a second order process involving four readout $4r$ photons occurring at a rate of 0.95 KHz, where the intermediate state energy is close to $E_i + 3\omega_r$.

10 This is a second order process involving two readout $2r$ photons occurring at a rate of 91 KHz. Fig. 5 also confirms that the transition 9 occurs with a higher probability compared to transition 8. The energy gap at the avoided crossing is

11 This is a first order process involving three readout photons ($3r$) occurring at a rate of 2.2 KHz.

12 This is a second order process involving two readout photons ($2r$) occurring at a rate of 52 KHz where $\Delta_{ac} = 1.1$ MHz.

Finally, we look at the transition rates for the $|\tilde{0}, \tilde{2}\rangle$, the state involved in the readout of a low-frequency fluxonium, shown in Fig. 14.

13 This is a second order process involving two-readout photons ($2r$) occurring at a rate of 16 (1) MHz which is the same as Δ_{ac} .

14 This is a second order process involving two-readout photons ($2r$) occurring at a rate of 2.2 KHz.

15 The first process is first order while the second process is second order, both involving ($1r$) and ($2r$) readout photons. The rates of these transitions are 1.48 KHz and 28 KHz, respectively. The energy gap at this avoided crossing is 4 MHz. Thus, this transition appears to be either a higher order process or a weaker transition.

4. Landau-Zener Probabilities

We compute the Landau-Zener probabilities numerically using the quasienergies from the Floquet simulations and analytically using the stark-shifted eigenenergies. In order to convert the Floquet simulation used with variation in \bar{n}_r at a fixed time t (ignoring the short scale fast dynamics over a time period), in this case, we will use a time-dependent case where \bar{n}_r varies as $\bar{n}_r = 50(1 - e^{-\kappa T/2})^2$ to emulate change in readout photons from dissipation. The numerical calculations use the probability for Landau-Zener transitions given in [29] for an avoided crossing observed between states i, f ,

$$P_{LZ} = \exp \left[-\pi \frac{\Delta_{ac}^2}{2v} \right], \quad (A6)$$

$$\text{where } v = \sqrt{2\Delta_{ac} \left| \frac{d^2 \epsilon_f}{d\bar{n}_r(t)^2} \right|_{t_{ac}}} \frac{d\bar{n}_r(t)}{dt} \Big|_{t_{ac}} \quad (A7)$$

Here, the variable ϵ_j is the numerically computed quasi-energy obtained from Floquet simulations, while Δ_{ac} refers to the quasi-energy difference at avoided crossing.

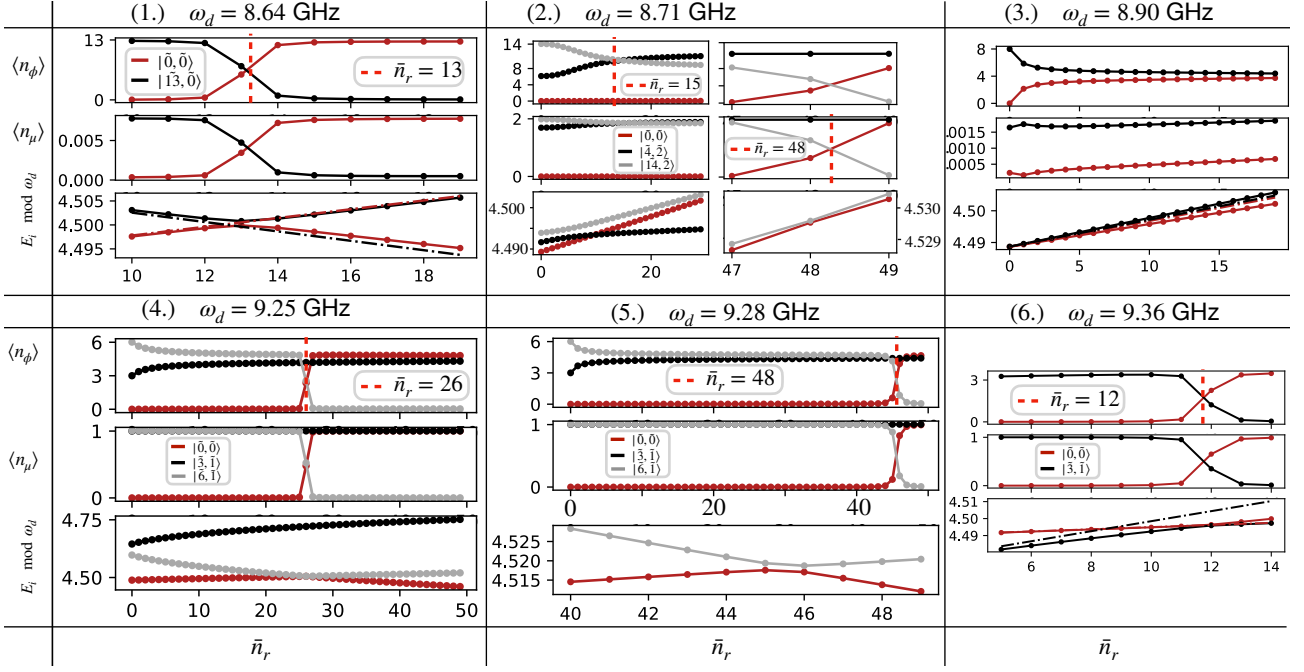


FIG. 12. MIST effects from Table III involving the $|\tilde{0}, \tilde{0}\rangle$ state. (Top row) Fluxonium subspace $\langle n_\phi \rangle$. (Middle) Parasitic mode subspace $\langle n_\mu \rangle$ (Bottom) Stark-shifted eigen-energies (dashed) and quasi-energies (solid) from Floquet simulations, corresponding to the initial state i as per the legend. Inset shows avoided crossing of quasi-energies. Floquet results are extracted from numerical data used for Fig. 3.

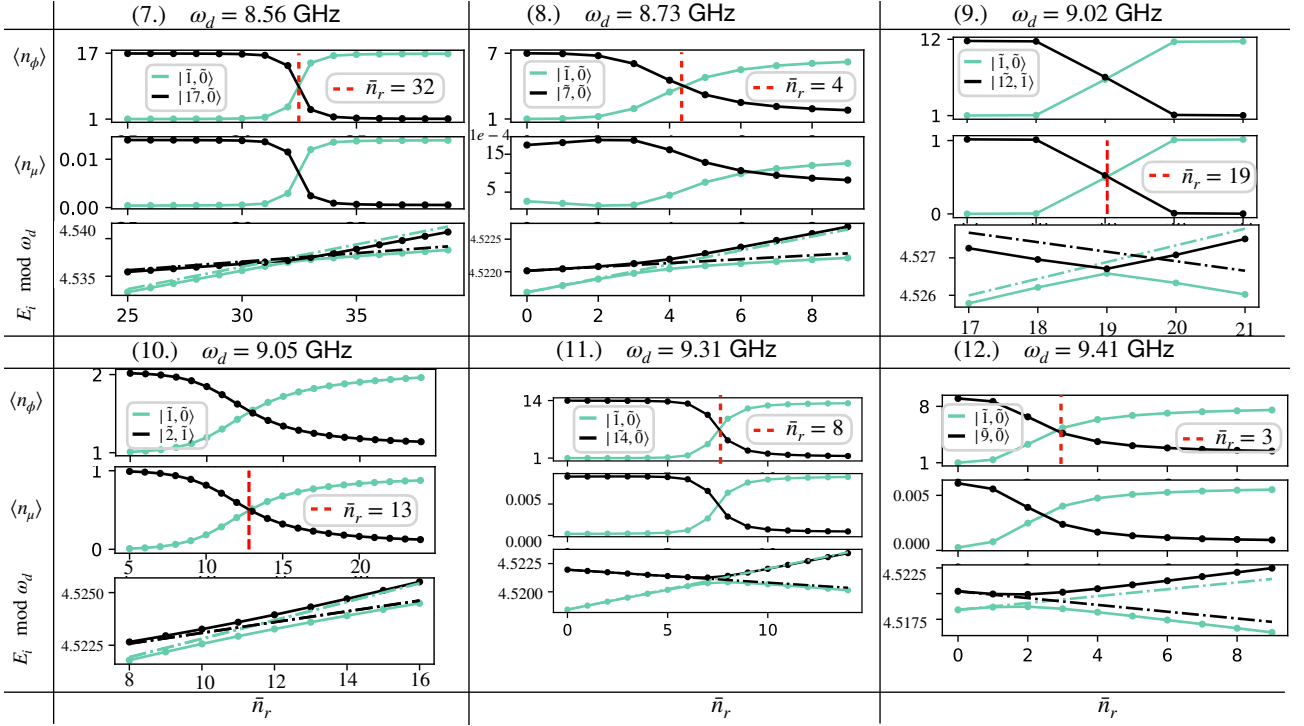


FIG. 13. MIST effects from Table III involving the $|\tilde{1}, \tilde{0}\rangle$ state. (Top row) Fluxonium subspace $\langle n_\phi \rangle$. (Middle) Parasitic mode subspace $\langle n_\mu \rangle$ (Bottom) Stark-shifted eigen-energies (dashed) and quasi-energies (solid) from Floquet simulations, corresponding to the initial state i as per the legend. Inset shows avoided crossing of quasi-energies. Floquet results are extracted from numerical data used for Fig. 3.

For the analytical calculations, we use the well-known formula (with energy in units of GHz),

$$P_{LZ} = \exp \left[-4\pi^2 \frac{V}{\frac{\partial \omega_{if}}{\partial \bar{n}_r(t)} \frac{d\bar{n}_r(t)}{dt}} \right], \quad (\text{A8})$$

$$\text{where } V = |\langle i | H_t | f \rangle|^2 \quad (\text{A9})$$

$$\omega_{if} = E_f + \chi_f(\bar{n}_r(t)) - E_i - \chi_i(\bar{n}_r(t)) \quad (\text{A10})$$

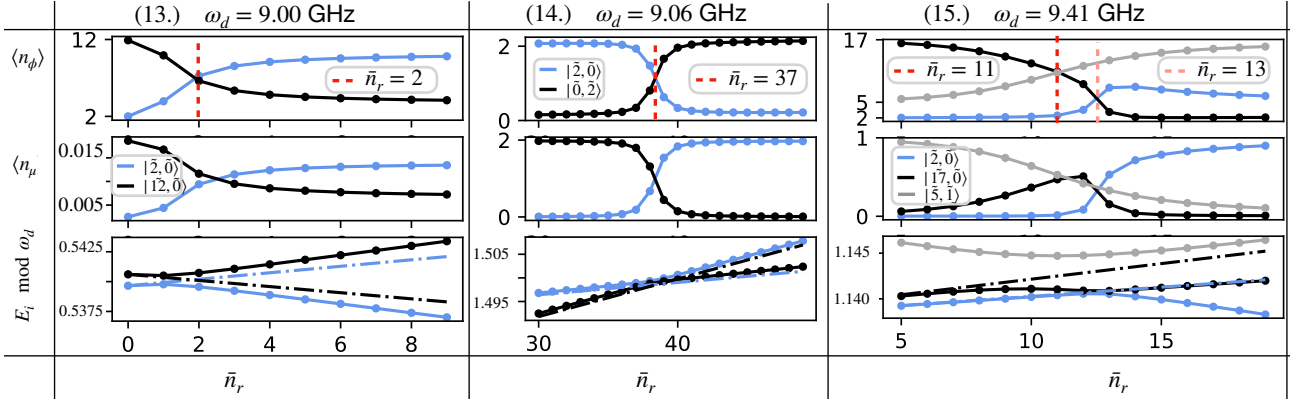


FIG. 14. MIST effects from Table III involving the $|\tilde{2}, \tilde{0}\rangle$ state. (Top row) Fluxonium subspace $\langle n_\phi \rangle$. (Middle) Parasitic mode subspace $\langle n_\mu \rangle$ (Bottom) Stark-shifted eigen-energies (dashed) and quasi-energies (solid) from Floquet simulations, corresponding to the initial state i as per the legend. Inset shows avoided crossing of quasi-energies. Floquet results are extracted from numerical data used for Fig. 3.

Here $\chi_i(\bar{n}_r(t)), \chi_f(\bar{n}_r(t))$ are ac stark shifts in the eigen-energies of i, j due to \bar{n}_r average readout photons. See app. A 2 for the calculation of these quantities.

5. Parasitic Dephasing

Any population in the parasitic modes can dephase the qubit via the interaction term $\chi_{\phi\mu} a_\mu^\dagger a_\mu \sigma_z$ in the dispersive Hamiltonian (see App. C). In this appendix, we lay out in detail our calculations of dephasing induced by the random occupation of the parasitic modes due to state transitions. We assume a scenario where the circuit is connected to a bath at $0K$ such that thermal photons can be set to $n_{th} = 0$. The parasitic mode is randomly populated to some non-zero \bar{n}_μ induced by the coupling of the readout with the parasitic mode. Now, at some point this population will go back to $\bar{n}_\mu = 0$ due to the decay of the parasitic modes dominated by the rate $\kappa_\mu = \frac{\omega_\mu}{Q_\mu}$. Here Q_μ, ω_μ are the quality factor and frequency of the parasitic mode. We are set to compute the dephasing due to the fluctuation in this quantity as the parasitic mode decays. We can compute the total decay rate of the parasitic modes as follows [37],

$$k_\mu = \kappa_r \frac{g_{\mu,r}^2}{\Delta^2} + \frac{\omega_\mu}{Q_\mu}, \quad (\text{A11})$$

where Δ is the detuning between the parasitic mode frequency and the readout drive frequency. The first terms and second terms depict contributions from Purcell effect due to the readout resonator ($\approx \text{Hz}$) and the quality factor Q_μ of the parasitic modes ($\approx \text{KHz-MHz}$). The second term dominates the expression and will determine the decay rate of the parasitic modes.

In this context, we use the methods described in Ref. [38] to compute the dephasing of a qubit given the initial occupation of the parasitic mode and the strong coupling between the qubit and the parasitic mode. Here, we use the dispersive Hamiltonian (see Eq. C4) of qubit-parasitic mode system, without the

readout. This assumption on the system is well-suited to cases where measurement has populated the parasitic mode. Even in the absence of any state transition in the fluxonium circuit, the parasitic mode is populated to $\bar{n}_\mu = \mathcal{O}(10^{-4})$ as shown in Fig. 7(a) due to the readout-parasitic mode coupling.

$$\frac{H}{\hbar} = \frac{\omega_q}{2} \sigma_z + \sum_\mu \left(\omega_\mu + k_\mu + \chi_{\mu\phi} \sigma_z \right) a_\mu^\dagger a_\mu, \quad (\text{A12})$$

$$+ \xi_{\mu r} \hat{N}_\phi \sin \omega_d t \quad (\text{A13})$$

where, κ_μ is the lamb shift, χ_μ is the stark shift, and ω_μ is the frequency of the parasitic mode. The variable ω_q denotes the qubit frequency i.e. the energy gap between the ground and the first excited state of the qubit potential. We ignore the qubit drive in this case since it will not play a role in the question of concern. In the presence of a qubit coupling, the state transitions will dominate the lifetimes and thus calculation of dephasing rates takes a backseat. In this scenario we are in the weak damping, strong coupling limit as $g_{\mu\phi}$ is of the order of GHz while the damping $\kappa_\mu = \frac{\omega_\mu}{Q_\mu}$ is of the order of MHz or KHz since all parasitic modes are designed to be high Q cavities. In the limit of zero temperature Ref. [38] shows that the dephasing rate coincides with what has been found in Ref. [37]. We use the calculations for the dispersive Hamiltonian (see Eq. C4 in App. C) to calculate for the drive-dependent dephasing rate at zero temperature quoted in [37, 38] assuming an initial \bar{n}_r .

$$\Gamma_\theta = \sum_\mu \frac{1}{2} \frac{|\xi_{\mu,r}|^2 \chi_{\mu,\phi}^2 \kappa_\mu}{[(\Delta + \chi_{\mu,\phi})^2 + (\kappa_\mu/2)^2]} \times \frac{1}{[(\Delta - \chi_{\mu,\phi})^2 + (\kappa_\mu/2)^2]} \quad (\text{A14})$$

$$= \sum_\mu \left[\frac{\chi_{\mu,\phi}^2 \kappa_\mu}{\Delta^2 + \kappa_\mu^2/4 + \chi_{\mu,\phi}^2} \right] \bar{n}_\mu, \quad (\text{A15})$$

Here, $\Delta = \omega_\mu - \omega_d$, χ_μ is the dispersive shift of the qubit due to the parasitic mode μ , and $\xi_{\mu,r} = 2g_{\mu,r} \sqrt{\bar{n}_r}$ is the drive strength of the parasitic mode in the semi-classical approximation.

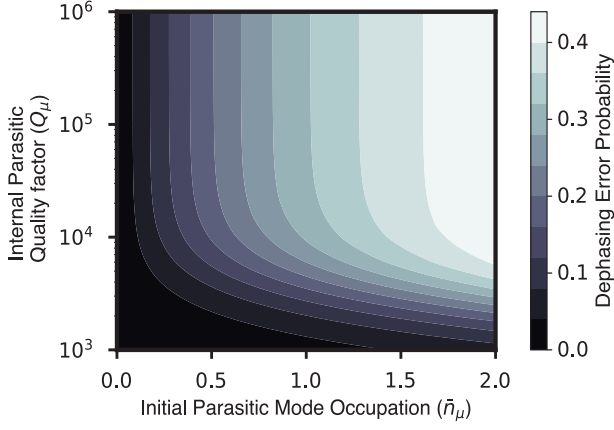


FIG. 15. Dephasing of the final qubit $1 - \langle \sigma_x \rangle_f = 2 \sin^2 \theta$ due to parasitic mode occupation from p-MIST effects after $t_f = 10/\kappa \mu$ s. The decay rate $\kappa = \omega_\mu/Q_\mu$ depends on the quality factor Q_μ and parasitic frequency ω_μ . The initial qubit state $|+\rangle = \frac{|g\rangle + |e\rangle}{\sqrt{2}}$ at $t_i = 0$ yields $\langle \sigma_x \rangle_i = 1$. Here, g, e denote the ground and excited qubit states. Parasitic mode occupation ranges from $\bar{n}_\mu = 0$ to $\mathcal{O}(1)$ average photons due to p-MIST effects. Over time, this decays to 0 given the quality factor Q_μ . Time evolution under the dispersive Hamiltonian $H = \chi_{\phi\mu} a_\mu^\dagger a_\mu \sigma_z$ and parasitic mode decay rate $\kappa_\mu = \frac{\omega_\mu}{Q_\mu}$ causes the qubit to dephase to $|\theta\rangle = \frac{|g\rangle + e^{i\theta}|e\rangle}{\sqrt{2}}$ due to the dispersive shift $\chi_{\phi\mu}$, which is 10 times larger than the qubit-readout dispersive shift.

Simulations using the dispersive Hamiltonian $\chi_{\phi\mu} a_\mu^\dagger a_\mu \sigma_z$ and decay $\sqrt{\kappa_\mu} \hat{a}_\mu$ reveal that significant dephasing can be induced due to these populated parasitic modes. The system is evolved for a time $t_f = 10/\kappa \mu$ s for various values of Q_μ . A higher Q_μ results in slower decay, setting a lower bound on the reset time needed to avoid parasitic-mode-induced dephasing.

Appendix B: Coupling Constant Landscape

Below is the dependence of charging energies and coupling constants on the number of junctions as well as the ground capacitance.

Appendix C: Undriven Fluxonium Circuit

In this appendix, we give the details of calculation and values (see Table IV) of the various circuits in Fig. 16(a-c). Throughout the document we quote energies in units of h i.e. GHz. We assume,

- $N = 122$
- $C_g^0 = C_g^N \neq C_g^i \quad \forall i \in [1, 2, \dots, N-1]$.
- capacitance between the transmission line and readout resonator is infinite, such that the readout resonator is at voltage V .

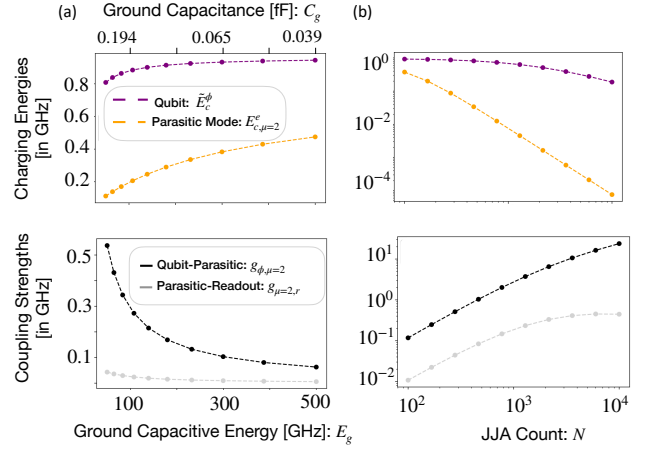


FIG. 16. The qubit charging energy in (a) decides the frequency and the parasitic charging energy in (b) decides the parasitic mode frequency. (c,d) give the plots for the coupling strengths of the parasitic mode to readout and qubit, respectively. All plots are obtained under linear JJA approximation. [SS: Add factor $1/2\pi$ for the coupling strengths notations in the legend. Also add plots for Will Oliver's parameters]

1. Circuit Features

- **Zero-point fluctuation of $e\hat{V}/h$:** We can use $eV = 2e^2(n_r/\sqrt{2})/C_r = 4E_{C_r}(n_r/\sqrt{2})$. If we absorb the factor of $4E_{C_r}$ in the coupling coefficient, then $\frac{n_{ZPF}}{\sqrt{2}} = \left(\frac{E_L}{8E_{C_r}}\right)^{1/4}$ and $e\hat{V} = 4E_{C_r}\hat{n}$. This is exactly equal to the quantity in Table IV[39].
- **Zero-point fluctuation of $n_{\phi,r}$:** For the qubit mode, we use the harmonic oscillator approximation where we define, $\frac{n_{ZPF}}{\sqrt{2}} = \left(\frac{E_J^j}{8NE_C^\phi}\right)^{1/4} = 1/\phi_{ZPF} \approx 0.36(H_1), 0.34(H_2), 0.34(H_3)$. This approximation holds correct if the convergence is taken care of using proper cutoff on this basis. The numbers quoted for chip 2(A&B) is 0.35.
- **Zero-point fluctuation of $n_{\mu,r}$:** For parasitic modes, it is $n_{ZPF} = \left(\frac{E_J^j}{8E_{C,\mu}^e}\right)^{1/4}$. We could use this to compute the absolute strengths for parasitic modes and resonator couplings.
- **Occupation Number of the Parasitic Modes:** As discussed in the main text, the parasitic mode frequencies are given by,

$$\omega_\mu^o = \sqrt{8E_{c,\mu}^o E_{J_j}} \quad (C1)$$

$$\omega_\mu^e = \sqrt{8E_{c,\mu}^e E_{J_j}} \quad (C2)$$

Here we have expressed ω for the case when energies are expressed in GHz. The thermal population of the parasitic modes can be calculated as $n = \frac{1}{e^{h\omega/kT} - 1}$ where k, T, f are the Boltzmann constant, temperature, and mode frequency, respectively. The frequency curve shown in Fig. 8

General Fluxonium Circuit	Phase-Slip Junction	Josephson-Junction Array
Ground capacitance	$C_g^0 = C_g^N = 10 - 20 fF$	$\{C_g^1, \dots, C_g^{N-1}\} = 0.05 - 0.1 fF$
Josephson Junction Energy	$E_{J_p} = 5 - 20 \text{GHz}$	$E_{J_j} = 40 - 100 \text{GHz}$
Capacitance Energy	$E_{C'} = 1 - 4 \text{GHz}$	$E_{C_j} = 50 fF / 115 E_{J_p} \text{GHz}$

Readout Circuit Parameters	Variables	Values
Readout Frequency	$\omega_r / 2\pi$	6-9 GHz
Resonator kappa	κ_r	1-15MHz (easy to tune)
Readout Impedance	$Z(\omega)$	$100/\pi$ or $200/\pi$
qubit-RO Coupling Capacitance (left)	$C_{c,1}$	1-2fF (Easy to tune)
qubit-RO Coupling Capacitance (right)	$C_{c,2}$	1-2fF (Easy to tune)
qubit frequency	ω_{01}	33.7MHz
plasmon frequency	ω_{12}	6.082GHz
dispersive shift (readout resonator)	χ_{RO}	0.5MHz for $g=20\text{MHz}$
Zero-point fluctuation of charge of resonator	$\phi_{r,ZPF}$	2.84
T_2^* limitation from 50mK resonator	T_2	8.9ms
coupling coefficient	$g_{r,\phi}$	26.1MHz
dispersive shift	χ_{01}	0.38MHz
dispersive shift	χ_{12}	0.125MHz
self-kerr	K_r	0.001MHz (averaged upto 10 photons)

Parameters	Variables	Set 1
Number of junctions in the array	N	122
Phase-Slip JJ energy	E_{J_p}	7.3 GHz
Target capacitance	$e^2/2(C_g + C')$	1GHz
Phase-Slip junction capacitance+differential capacitance	$E_{C'}$	$(1 - 2/E_{g,p})^{-1} \text{GHz}$
JJA junction energy	E_{J_j}	60 GHz
JJA capacitance energy	E_{C_j}	0.74GHz
JJA ground capacitance	$E_{g,j}$	194 GHz
Phase-slip parasitic ground capacitance	$E_{g,p}$	1.94 GHz
Coupling capacitance	E_c	19.4 GHz
Readout loss rate	κ_r	1MHz
Readout Frequency	$\omega_r / 2\pi$	8.5GHz
Quality-Factor	Q	8500
Zero-point fluctuation of charge operator	n_{ZPF}	1.4
Zero-point fluctuation of phase operator	ϕ_{ZPF}	0.357

TABLE IV. Circuit Parameters. Capacitive energies E_g, E_c , etc.. are determined using $E_c = (e^2/2hC) = \frac{1.94e-5}{C} = 19.4/C(fF)[\text{GHz}]$.

saturates at 18.8 GHz while the occupation number of the lowest even (odd) mode stands at 12.06 (7.25). Only the even modes couple to the readout and parasitic modes. The occupation number of the first even (odd) mode is $9.3e - 6$ ($9e - 4$). The highest mode saturates at an occupation number of $1.4e - 8$. Importantly, For a temperature of $20mK$, the lowest odd mode population is down to $6.3e - 8$.

2. Qubit Hamiltonian: H_ϕ

The qubit Hamiltonian H_ϕ is diagonalized in the Fock state basis but a better strategy would be to diagonalize this Hamiltonian in the Kerr-cat basis. For the harmonic oscillator basis, we have used $\hat{x} = x_{zpf} \frac{a+a^\dagger}{\sqrt{2}}$ while $\hat{p} = p_{zpf} \frac{a-a^\dagger}{i\sqrt{2}}$, where $x_{zpf} = p_{zpf}^{-1}$. If instead we use $\hat{x} = x_{zpf}(a+a^\dagger)$ and $\hat{p} = -ip_{zpf}(a-a^\dagger)$, then $x_{zpf} = \frac{1}{2p_{zpf}}$. Each zero-point fluctuation value in the two cases is related as $ZPF_2 = ZPF_1/\sqrt{2}$. Emma's calculations use the latter definition.

a. Energy Spectrum for H_1 : The Hamiltonian of the qubit subspace is $H_\phi = 4\tilde{E}_C n_\phi^2 + E_{J,p} \cos \phi + \frac{1}{2} E_L \phi^2$, where $E_L = \frac{E_g^a}{N}$. The zero-point fluctuation of the unit-less phase operator ϕ is $n_{ZPF,\phi}^{-1} = 1.39$. This matches with Emma's calculations where this value is 1.4.

b. Charge Matrix Elements for H_1, H_2, H_3 : Here, using the approximations described in the appendix, we get the following charge matrix elements for the qubit subspace.

3. Dispersive Hamiltonian

Using Schrieffer-Wolff approximation, we can write the Hamiltonian for the qubit subspace as follows [26],

$$2\pi H = \frac{\omega_q}{2} \sigma_z + \sum_{\mu} (\omega_{\mu} + k_{\mu}) a_{\mu}^{\dagger} a_{\mu} + \omega_r a_r^{\dagger} a_r + \chi_{r,\phi} \sigma_z a_r^{\dagger} a_r + \sum_{\mu} \chi_{\mu,\phi} \sigma_z a_{\mu}^{\dagger} a_{\mu}$$

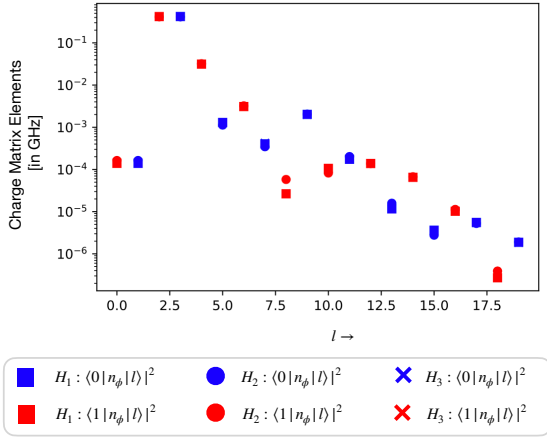


FIG. 17. Charge Matrix Elements (squared) for all three circuits. Note that in the equations below we substitute $\langle l|n|l' \rangle = in_{ZPF} \langle l|a - a^\dagger|l' \rangle$ where $n_{ZPF} = \frac{1}{\sqrt{2}} \left(E_{J,j} / 8NE_C \right)^{1/4}$. The charge matrix elements between odd-odd or even-even is zero (points not seen in log plot) due to the symmetry of cosine potential at $\varphi_{ext} = 0.5\Phi_0$, where Φ_0 is the flux quantum.

$$+ \sum_{\mu} \chi_{r\mu} a_{\mu}^{\dagger} a_{\mu} a_r^{\dagger} a_r \quad (C3)$$

$$= \frac{\omega_q}{2} \sigma_z + \left(\omega_r + \chi_{r\phi} \sigma_z \right) a_r^{\dagger} a_r + \sum_{\mu} \left(\omega_{\mu} + k_{\mu} + \chi_{r\mu} a_{\mu}^{\dagger} a_r + \chi_{\mu\phi} \sigma_z \right) a_{\mu}^{\dagger} a_{\mu} \quad (C4)$$

where ω_q or $\omega_{01} = \epsilon_0 - \epsilon_1$

$$+ |\langle 0|p_{\phi}|1 \rangle|^2 \left[16g_{r\phi}^2 E_{C_r}^2 \sqrt{\frac{E_{L_r}}{32E_{C_r}}} \frac{2\epsilon_{01}}{\epsilon_{01}^2 - \omega_r^2} + \sum_{\mu} \left\{ g_{\mu\phi}^2 \sqrt{\frac{E_J^j}{32\tilde{E}_{C,\mu}^e}} \frac{2\epsilon_{01}}{\epsilon_{01}^2 - \omega_{\mu}^2} \right\} \right] + \sum_{l>1} 16g_{r\phi}^2 E_{C_r}^2 \sqrt{\frac{E_{L_r}}{32E_{C_r}}} \left[\frac{|\langle 0|p_{\phi}|l \rangle|^2}{\epsilon_{0l} - \omega_r} - \frac{|\langle 1|p_{\phi}|l \rangle|^2}{\epsilon_{1l} - \omega_r} \right] + \sum_{l>1,\mu} \left\{ g_{\mu\phi}^2 \sqrt{\frac{E_J^j}{32\tilde{E}_{C,\mu}^e}} \times \left[\frac{|\langle 0|p_{\phi}|l \rangle|^2}{\epsilon_{0l} - \omega_{\mu}} - \frac{|\langle 1|p_{\phi}|l \rangle|^2}{\epsilon_{1l} - \omega_{\mu}} \right] \right\} \quad (C5)$$

$$k_{\mu \in 2\mathbb{Z}} = 16E_{C_r}^2 \sqrt{\frac{E_{L_r}}{32E_{C_r}}} \sqrt{\frac{E_J^j}{32E_C^e}} \left[\frac{g_{r\mu}^2}{\omega_{\mu} - \omega_r} \right] \leq \mathcal{O}(10^{-8}) \quad (C6)$$

$$\chi_{r,\phi} = 16g_{r\phi}^2 E_{C_r}^2 \sqrt{\frac{E_{L_r}}{32E_{C_r}}} \frac{2\epsilon_{01}}{\epsilon_{01}^2 - \omega_r^2} |\langle 0|p_{\phi}|1 \rangle|^2 + 16g_{r\phi}^2 E_{C_r}^2 \sqrt{\frac{E_{L_r}}{32E_{C_r}}} \left[\sum_l |\langle 0|p_{\phi}|l \rangle|^2 \frac{\epsilon_{0l}}{\epsilon_{0l}^2 - \omega_r^2} - \sum_l |\langle 1|p_{\phi}|l \rangle|^2 \frac{\epsilon_{1l}}{\epsilon_{1l}^2 - \omega_r^2} \right] \quad (C7)$$

$$\chi_{\mu,\phi} = g_{\mu\phi}^2 \sqrt{\frac{E_J^j}{32\tilde{E}_{C,\mu}^e}} \frac{2\epsilon_{01}}{\epsilon_{01}^2 - \omega_{\mu}^2} |\langle 0|p_{\phi}|1 \rangle|^2 + g_{\mu\phi}^2 \sqrt{\frac{E_J^j}{32\tilde{E}_{C,\mu}^e}} \left[\sum_l |\langle 0|p_{\phi}|l \rangle|^2 \frac{\epsilon_{0l}}{\epsilon_{0l}^2 - \omega_{\mu}^2} - \sum_l |\langle 1|p_{\phi}|l \rangle|^2 \frac{\epsilon_{1l}}{\epsilon_{1l}^2 - \omega_{\mu}^2} \right] \quad (\text{see Fig. 18}) \quad (C8)$$

Therefore $\omega_q = -7e - 04$ GHz, $\omega_{q,r} = -1.1e - 03$ GHz, see Fig. 18 for $\omega_{q,\mu}$, $\chi_{\mu,\phi}$.

The dispersive shift between the qubit and the readout is small due to the small charge matrix elements. The primary element which contributes to this quantity is the 03 and 12 transitions. The dispersive shift between the qubit and the parasitic modes follows.

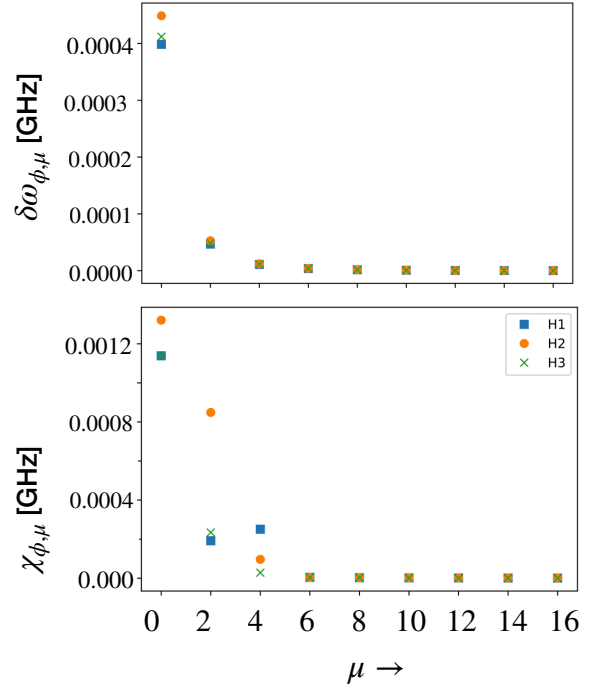


FIG. 18. All values are in $\frac{GHz}{2\pi}$ units. The color code follows: H_1 (blue), H_2 (orange), H_3 (green) for the three circuits shown in Fig. 16(a-c). (Top) Change in the qubit frequency due to parasitic mode μ (Bottom) Dispersive shift χ_{μ} of the qubit concerning the parasitic mode μ .

Appendix D: Single-Point Connections

We find that, if the differential capacitance C and coupling capacitance C_c are altered such that qubit frequency and qubit-readout coupling are same across all three circuits, the parasitic mode effects are bound to have the same effect given our assumptions of ordered array and no self-nonlinearity in parasitic modes. To emphasize this, we plot the three types of coupling strengths across all circuits in Fig. 19 while other parasitic parameters are given in Table. V. Note that, this symmetry prevents any coupling with the lowest-

Fluxonium Parameters ($\mu = 2$)	H_1 Parallel Circuit	H_2 Floating Fluxonium	H_3 Grounded Circuit
$g_{\phi\mu}$	157 GHz	161 GHz	158 GHz
$g_{\mu r}$	4.223 MHz	3.971 MHz	3.128 MHz
$\chi_{\phi,\mu}$	-1.1 MHz	-1.3 MHz	-1.1 MHz
$\delta\omega_{01,\mu}$	0.4 MHz	0.45 MHz	0.41 MHz

TABLE V. Fluxonium parameters with the lowest frequency parasitic mode with non-zero coupling to the qubit and readout $\mu = 2$. Here we quote the frequency of the fluxon transition between the lowest two levels (ω_{01}) and the plasmon transition between the first and second levels (ω_{12}). For the dispersive Hamiltonian obtained for each circuit (see App. D), we quote the dispersive shift due to readout as χ_r . The values in this table have been experimentally verified for H_1 . The frequency of this mode is $f_\mu = 12.063$ GHz. We give the coupling strengths between the qubit-readout $g_{\phi\mu}$, readout-parasitic $g_{\phi r}$, parasitic-qubit $g_{\mu r}$ modes. We also give the stark shift $\chi_{\phi\mu}$ and frequency correction $\delta\omega_{01,\mu}$ on the two-level system realized by this fluxonium circuit in the dispersive regime. Here the values of $g_{\phi r}$, $\chi_{\phi r}$, $\omega_{\mu=2}$ have been verified experimentally for H_1 .

frequency parasitic mode ($\mu = 1$), presence of which would be potentially detrimental.

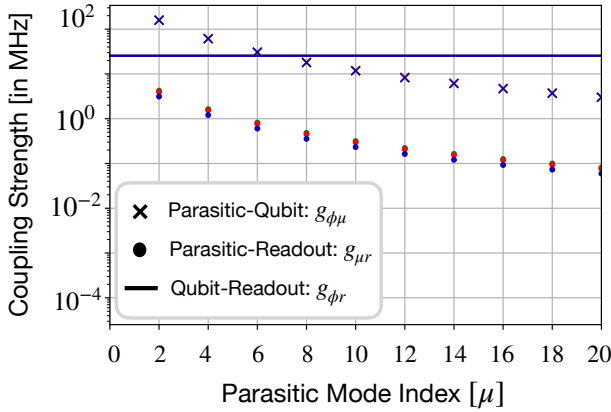


FIG. 19. Absolute values of the coupling strengths in GHz for various circuits. H_1 (green): Parallel circuit (see Fig. 2), H_2 (blue): single-Point connection with floating fluxonium (see Fig. 20 (b)), and H_3 (red): single-Point Connection with grounded fluxonium (see Fig. 20 (c)). The behavior for all circuits is the same, thus the discussion in the main text focused on H_1 can be easily extended to H_2, H_3 . Coupling to odd parasitic modes is zero due to the symmetries of the circuit [26].

The fluxonium readout circuit shown can have several modifications and each can affect various parameters associated with the efficiency of a fluxonium readout circuit as we proceed to show in this work. Here, in Fig. 16 we present two modifications to the parallel circuit shown in Fig. 2 with different grounding options for the fluxonium circuit. We will refer to these three circuit choices as H_1 : (Parallel circuit, see circuit in Fig. 2), H_2 : (Floating fluxonium, see left circuit in Fig. 16), H_3 : (Grounded fluxonium, see right circuit in Fig. 16). Note that each parameter in Table. V is significantly different for the three circuits.

We adjust the coupling capacitance C_c and the total capacitance of the phase slip junction E_{C_p} (by modifying C') to achieve the same qubit frequency ω_{01} , plasmon frequency ω_{23} , qubit-readout coupling constant $g_{\phi\mu}$ and qubit-readout dispersive shift $\chi_{\phi r}$ for the three circuits as given in Table II. These modifications yield for circuit (b) $E_{C_p} = 0.83$ GHz, $E_{C_c} = 3.82$ GHz (c) $E_{C_p} = 0.80$ GHz, $E_{C_c} = 4.70$ GHz. Table. V gives values of the various circuit parameters across the three circuits computed analytically using the expressions given in Sec. IV and App. D. We note that upon adjusting the qubit parameters, all circuit parameters are similar in the three circuits. Hence, we do not expect any change in the MIST/p-MIST effects for single-point connected circuits in the hangar geometry in comparison to what has already been shown in this work.

Here we will follow the recipe of Ref. [26] to derive Hamiltonians for circuits shown in Figs. 16(b,c). We will use the following notations defined in Table IV. The Lagrangian corresponding to these circuits is a combination of the Lagrangians, \mathcal{L}_g from the phase-slip junction (comprising of the junction with $E_J/E_C \sim 5 - 8$ and the capacitor C), \mathcal{L}_g from the ground capacitances, \mathcal{L}_{RO} from the readout resonator and \mathcal{L}_c due to the coupling capacitances C_c and the external voltage V . We mark the flux points across JJA using φ_0 and φ_N . We write the capacitive energy terms using $E_x = \frac{e^2}{2C_x}$ and the voltages of each island $\varphi/2e$, such that, $\frac{1}{2}C\frac{\varphi^2}{4e^2} = \frac{\varphi^2}{16E_C}$. For simplicity, we have $C_{g,i} = C_g \forall i$. The flux variables and voltage variables in the circuit are denoted by $\varphi_n = 2\pi\Phi_n/\Phi_0$ and $\dot{\varphi}_n = 2\pi V_n/\Phi_0$, respectively, where $\Phi_0 = h/2e$ is the superconducting flux quantum. We will use subscripts j, p for JJA and the phase-slip junction coordinates, respectively. The capacitance associated with the phase-slip junction is given by $\frac{1}{E_{C'}} = \frac{1}{E_C} + \frac{1}{E_C^j}$.

1. Trends in Circuit Variables

1. Total ground capacitance.

$$(a) H_2 : E_t = \left(\frac{N-1}{E_{g_j}} + \frac{2}{E_{g_p}} + \frac{1}{E_c} \right)^{-1}$$

$$(b) H_3 : E_t = \left(\frac{N-1}{E_{g_j}} + \frac{1}{E_{g_p}} + \frac{1}{E_c} \right)^{-1}$$

2. Qubit Charging energy ($4E_c^{\phi}\hat{N}_{\phi}^2$).

$$(a) H_2 : \bar{E}_c^{\phi} = \left(\frac{1}{4E_t} \left(1 - \frac{E_t}{E_c} \right)^2 \left[1 - \frac{2}{3} \frac{N-1}{N} \right] + \frac{1}{E_{C_p}} + \frac{1}{N E_{C_j}} \right)^{-1}.$$

$$(b) H_3 : \bar{E}_c^{\phi} = \left(\frac{1}{4E_t} \left(1 - \frac{E_t}{E_c} \right)^2 \left[1 - \frac{2}{3} \frac{N-2}{N-1} \right] + \frac{1}{E_{C_p}} + \frac{1}{N E_{C_j}} \right)^{-1}.$$

3. Even Parasitic Mode Charging Energy ($4E_{c,\mu}^e\hat{N}_{\mu}^2$).

$$(a) H_2 : \text{Same as } H_1$$

$$(b) H_3 : \text{Same as } H_1$$

4. Qubit-Readout Coupling ($g_{\phi r}\hat{N}_{\phi}\hat{N}_{\mu}$).

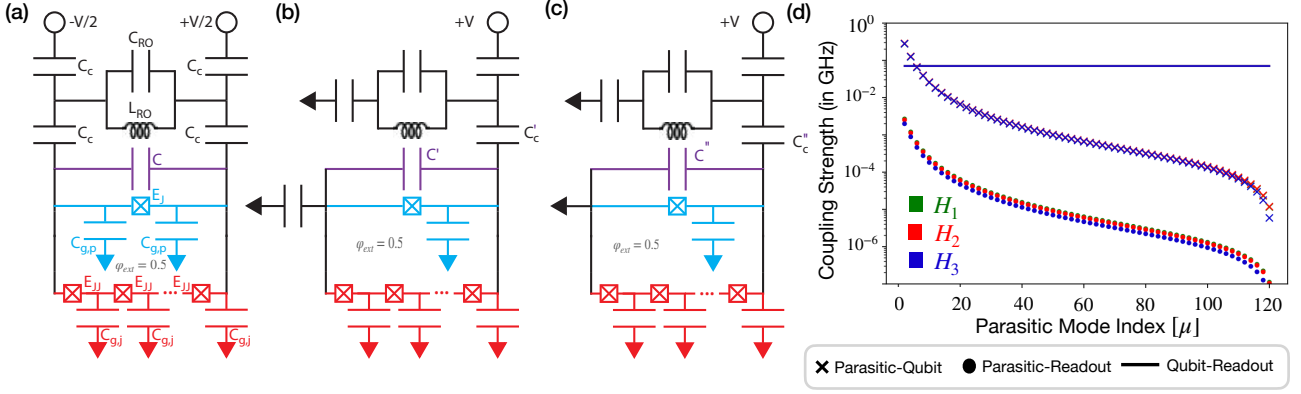


FIG. 20. (a-c) Alternative readout circuits. (a) Parallel circuit, (b) Floating fluxonium, (c) Grounded fluxonium. Alternatives (b) and (c) require a single-point connection to the readout line \$V\$, unlike the parallel circuit in (a). We maintain the values for all circuit variables the same as used for the case of the parallel circuit in Fig. 2. (d) Absolute values of the coefficients of coupling terms in the Hamiltonian (in GHz). We can see that the parasitic modes couple to the qubit stronger than the qubit couples to the readout. The parasitic mode coupling to the readout is very slightly weaker in \$H_3\$ compared to \$H_1, H_2\$.

$$\begin{aligned}
 (a) \quad H_1 &: \frac{\tilde{E}_c^\phi}{E_c} \\
 (b) \quad H_2 &: \frac{\tilde{E}_c^\phi}{E_c} \left[\frac{(N+1)E_t}{2E_{g_j}} + \frac{E_t^2 \tilde{E}_{c,\mu}^o}{8E_{g_j}^2 E_c} \left(\frac{c_\mu^2}{2Ns_\mu^4} \right) \right] \\
 (c) \quad H_3 &: \frac{\tilde{E}_c^\phi}{E_c} \left[\frac{NE_t}{2E_{g_j}} + \frac{E_t^2 \tilde{E}_{c,\mu}^o}{8E_{g_j}^2 E_c} \left(\frac{c_\mu^2}{2(N-1)s_\mu^4} \right) \right]
 \end{aligned}$$

5. Qubit-Parasitic Coupling (\$g_{\phi\mu}\hat{N}_\phi\hat{N}_\mu\$)

$$\begin{aligned}
 (a) \quad H_1 &: \sqrt{\frac{2}{N}} \frac{\tilde{E}_c^\phi \tilde{E}_{c,\mu}^e c_\mu}{E_{g_j} s_\mu^2} \\
 (b) \quad H_2 &: \sqrt{\frac{2}{N}} \frac{\tilde{E}_c^\phi \tilde{E}_{c,\mu}^e c_\mu}{E_{g_j} s_\mu^2} \\
 (c) \quad H_3 &: \sqrt{\frac{2}{N-1}} \frac{\tilde{E}_c^\phi \tilde{E}_{c,\mu}^e c_\mu}{E_{g_j} s_\mu^2}
 \end{aligned}$$

6. Readout-Parasitic Coupling (\$g_{\mu r}\hat{N}_\mu\hat{N}_r\$)

$$\begin{aligned}
 (a) \quad H_1 &: \frac{\tilde{E}_c^\phi \tilde{E}_{c,\mu}^e c_\mu}{4\sqrt{2N}E_{g_j} E_c s_\mu^2} \\
 (b) \quad H_2 &: \frac{\tilde{E}_c^\phi \tilde{E}_{c,\mu}^e c_\mu}{4\sqrt{2N}E_{g_j} s_\mu^2 E_c} \left[\frac{(N+1)E_t}{2E_{g_j}} \right] \\
 (c) \quad H_3 &: \frac{\tilde{E}_c^\phi \tilde{E}_{c,\mu}^e c_\mu}{4\sqrt{2(N-1)}E_{g_j} s_\mu^2 E_c} \left[\frac{NE_t}{2E_{g_j}} \right]
 \end{aligned}$$

2. Floating Fluxonium Circuit: \$H_2\$

Transforming the Lagrangian in Ref. [26], the following terms will remain the same in the case of floating fluxonium circuit, given the diagrams in the following sections.

$$\mathcal{L} = \mathcal{L}_{\text{phase-slip}} + \mathcal{L}_{JJA} + \mathcal{L}_g + \mathcal{L}_{RO} + \mathcal{L}_C \quad (D1)$$

$$\mathcal{L}_{\text{phase-slip}} = \frac{(\dot{\varphi}_N - \dot{\varphi}_0)^2}{16E_C} - E_{J_p} \cos(\varphi_0 - \varphi_N + \varphi_{ext}) \quad (D2)$$

$$\mathcal{L}_{JJA} = \sum_{n=1}^N \frac{(\dot{\varphi}_n - \dot{\varphi}_{n-1})^2}{16E_{C_j}^n} - E_{J_j}^n \cos(\varphi_n - \varphi_{n-1}) \quad (D3)$$

$$\mathcal{L}_{RO} = \frac{\dot{\varphi}_-^2}{16E_{RO}} - \frac{\varphi_-^2}{16E_{RO}} \quad (D4)$$

$$\mathcal{L}_g = \sum_{n=0}^N \frac{\dot{\varphi}_n^2}{16E_g^n} \quad (D5)$$

Here, we will not assume that the capacitances to transmission line are infinite or that ground capacitance for the phase-slip junction and JJA. We will leave the value of \$\varphi_\pm\$ a variable in this case unlike the parallel circuit study we performed above.

$$\mathcal{L}_c = \frac{(\dot{\varphi}_{-1} - \dot{\varphi}_0)^2}{16E_c^1} + \frac{(\dot{\varphi}_{-1} - eV)^2}{16E_c^3} + \frac{(\dot{\varphi}_{-2})^2}{16E_c^4}, \quad (D6)$$

$$\begin{aligned}
 &= \frac{\dot{\varphi}_0^2}{16E_c^1} + \frac{\dot{\varphi}_{-1}^2}{16} \left(\frac{1}{E_c^1} + \frac{1}{E_c^3} \right) + \frac{\dot{\varphi}_{-2}^2}{16E_c^4} \\
 &\quad - \frac{\dot{\varphi}_0 \dot{\varphi}_{-1}}{8E_c^1} - \frac{\dot{\varphi}_{-1} eV}{8E_c^3} + \mathcal{O}(V^2)
 \end{aligned} \quad (D7)$$

Here, \$E_c^4\$ is the capacitance via which the readout resonator is grounded. Using the basis of (gauge-invariant) phase difference,

$$\varphi_m - \varphi_0 = \sum_{l=1}^m \theta_l \quad (D8)$$

$$\sum_{m=0}^N \theta_m + \varphi_{ext} = 2\pi z, \quad z \in \mathbb{Z} \quad \text{“fluxoid quantization”} \quad (D9)$$

$$\varphi_{ext} = \pi, \quad (D10)$$

a. *Lagrangian* From using Eq. D5, we find that,

$$\dot{\varphi}_0 = E_t \left(\frac{\dot{\varphi}_{-1}}{E_c^1} - \sum_{n=1}^N \sum_{m=n}^N \frac{\dot{\theta}_n}{E_g^m} \right) \quad (D11)$$

$$\text{where } E_t = \left(\frac{1}{E_c^1} + \sum_{n=0}^N \frac{1}{E_g^n} \right)^{-1}$$

$$\therefore \mathcal{L}_g + \mathcal{L}_c = \frac{\dot{\varphi}_{-1} eV}{8E_c^3} + \frac{\dot{\varphi}_{-1}^2}{16} \left(\frac{1}{E_c^1} \left(1 - \frac{E_t}{E_c^1} \right) + \frac{1}{E_c^3} \right)$$

$$\begin{aligned}
& + \sum_{n=1}^N \frac{\dot{\varphi}_{-1} \dot{\theta}_n}{E_c^1} \left(\sum_{i=n}^N \frac{E_t}{8E_g^i} \right) \\
& + \sum_{m=1}^N \sum_{n=1}^N \dot{\theta}_m \dot{\theta}_n \left(\sum_{j=\max\{m,n\}}^N \frac{1}{16E_g^j} \right) \\
& \left(1 - \sum_{i=\min\{m,n\}}^N \frac{E_t}{E_g^i} \right) \quad (D12)
\end{aligned}$$

We simplify the Lagrangian $\mathcal{L}_g + \mathcal{L}_c$ as

$$\begin{aligned}
& = \frac{\dot{\varphi}_{-1} eV}{8E_c} + \frac{\dot{\varphi}_{-1}^2}{16} \left(\frac{1}{E_c} \left(1 - \frac{E_t}{E_c} \right) + \frac{1}{E_c} \right) \\
& + \sum_{n=1}^N \left(\frac{\dot{\varphi}_{-1} \dot{\theta}_n}{E_c} \right) (N - n + 1) \frac{E_t}{8E_g} + \frac{(\dot{\varphi}_{-2})^2}{16E_c^4} \\
& + \sum_{m=1}^N \sum_{n=1}^N \dot{\theta}_m \dot{\theta}_n \frac{(N - \max\{m, n\} + 1) \min\{m, n\} E_t}{16E_g^2} \quad (D13)
\end{aligned}$$

This expansion shows that the parasitic couplings depend on the ground capacitance due to terms like $\dot{\theta}_m \dot{\theta}_n$ while the coupling capacitance comes into picture only via couplings with the readout resonator mode.

b. Collective Modes We now transform to a new set of variables $\{\phi, \zeta_1, \dots, \zeta_{N-1}\}$, also known as the difference modes μ and their amplitudes ξ_μ ,

$$\theta_m = \phi/N + \sum_{\mu} W_{\mu m} \xi_{\mu}, \quad (D14)$$

and inversely,

$$\phi = \sum_m \theta_m, \quad \xi_{\mu} = \sum_m W_{\mu m} \theta_m. \quad (D15)$$

Here, ϕ is the superinductance mode where all array junction amplitudes are identical. The difference modes ξ_{μ} are such that the amplitude sum for all difference modes vanishes. See figures in [15]. The matrix $(N-1) \times N$ matrix W is semi-orthogonal, $\sum_m W_{\mu m} W_{\nu m} = \delta_{\mu\nu}$ and its row sum is zero, $\sum_m W_{\mu m} = 0$. Thus, the following choice is observed in [15] and later used in [26]

$$W_{\mu m} = \sqrt{\frac{2}{N}} \cos \frac{\pi \mu (m - 1/2)}{N}. \quad (D16)$$

The choice of these new variables is to identify the collective modes describing the low-energy physics as illustrated in [25, 40, 41]. Thus, under these new set of variables which define the normal modes of oscillations in θ_m , we have,

$$\mathcal{L} = \mathcal{T} - \mathcal{U} \quad (D17)$$

$$\begin{aligned}
\mathcal{T} & = \frac{\dot{\varphi}_{-1} eV}{8E_c^3} - \frac{\dot{\varphi}_{-2} eV}{8E_c^4} - E_t \frac{\dot{\varphi}_{-1} \dot{\varphi}_{-2}}{8E_c^2} \\
& + \frac{\dot{\varphi}_{-1}^2}{16} \left(\frac{1}{E_c} \left(1 - \frac{E_t}{E_c} \right) + \frac{1}{E_c^3} \right) + \frac{\dot{\varphi}_{-2}^2}{16} \left(\frac{1}{E_c^4} + \frac{1}{E_c} \left(1 - \frac{E_t}{E_c} \right) \right) \\
& + \left[\sum_{n=1}^N \left(\frac{\dot{\varphi}_{-1}}{E_c} + \frac{\dot{\varphi}_{-2}}{E_c} \right) \left(\frac{E_t}{8E_c} + (N - n + 1) \frac{E_t}{8E_g} \right) \right.
\end{aligned}$$

$$\begin{aligned}
& \left. - \sum_{n=1}^N \frac{\dot{\varphi}_{-2}}{8E_c} \right] \left(\dot{\phi}/N + \sum_{\mu} W_{\mu n} \dot{\xi}_{\mu} \right) + \sum_{m=1}^N \sum_{n=1}^N \left(\dot{\phi}/N \right. \\
& \left. + \sum_{\mu} W_{\mu n} \dot{\xi}_{\mu} \right) \left(\dot{\phi}/N + \sum_{\mu} W_{\mu m} \dot{\xi}_{\mu} \right) \left((N - \max\{m, n\} \right. \\
& \left. + 1) \frac{1}{16E_g} + \frac{1}{16E_c} \right) \left(\min\{m, n\} \frac{E_t}{E_g} + \frac{E_t}{E_c} \right) \quad (D18)
\end{aligned}$$

$$\begin{aligned}
\mathcal{U} & = -E_{J_p} \cos(\phi) - \frac{(\varphi_{-1} - \varphi_{-2})^2}{16E_{RO}} \\
& - \sum_{n=1}^N E_{J_j} \cos \left(\phi/N + \sum_{\mu} W_{\mu n} \xi_{\mu} \right) \quad (D19)
\end{aligned}$$

c. Symmetries in the Lagrangian Simplifying the kinetic energy term from Eq. D18 using $\sum_m W_{\mu m} = 0$ and the semi-orthogonal matrix condition $\sum_m W_{\mu m} W_{\nu m} = \delta_{\mu\nu}$ used above yields,

$$\begin{aligned}
\mathcal{T} & = -\frac{\dot{\varphi}_{-2} eV}{16E_c} + \frac{\dot{\varphi}_{-1} eV}{16E_c} - E_t \frac{\dot{\varphi}_{-1} \dot{\varphi}_{-2}}{16E_c^2} \\
& + \frac{\dot{\varphi}_{-1}^2}{16} \left(\frac{1}{E_c} \left(1 - \frac{E_t}{E_c} \right) + \frac{1}{E_c} \right) + \frac{\dot{\varphi}_{-2}^2}{16} \left(\frac{1}{E_c} + \frac{1}{E_c} \left(1 - \frac{E_t}{E_c} \right) \right) \\
& + \frac{E_t}{8E_c^2} \dot{\varphi}_{-1} \dot{\phi} + \frac{E_t}{8E_c^2} \dot{\varphi}_{-2} \dot{\phi} \\
& + \left[\sum_{n=1}^N \left(\frac{\dot{\varphi}_{-1}}{E_c} + \frac{\dot{\varphi}_{-2}}{E_c} \right) \left(\frac{E_t}{8E_c} + (N - n + 1) \frac{E_t}{8E_g} \right) \right. \\
& \left. - \sum_{n=1}^N \frac{\dot{\varphi}_{-2}}{8E_c} \right] \left(\dot{\phi}/N + \sum_{\mu} W_{\mu n} \dot{\xi}_{\mu} \right) \\
& + \left[(M_{00} + G_{00}) \dot{\phi}^2 + 2 \sum_{\mu} (M_{0\mu} + G_{0\mu}) \dot{\phi} \dot{\xi}_{\mu} \right. \\
& \left. + \sum_{\mu, \nu} (M_{\mu\nu} + G_{\mu\nu}) \dot{\xi}_{\mu} \dot{\xi}_{\nu} \right] \quad (D20)
\end{aligned}$$

Here M comes from the phase-slip junction and JJA while G comes from the coupling and ground capacitances, and these coefficients are given by,

$$M_{00} = \frac{1}{16E_{C'}} + \frac{1}{16NE_{C_j}}, \quad M_{0\mu} = 0, \quad M_{\mu\nu} = \frac{\delta_{\mu\nu}}{16E_{C_j}} \quad (D21)$$

$$G_{00} = \frac{1}{64E_t} \left(1 - \frac{E_t}{E_c} \right)^2 \left[1 - \frac{2}{3} \frac{N-1}{N} \right] \quad (D22)$$

$$G_{0\mu} = -\frac{c_{\mu} o_{\mu+1}}{16E_g \sqrt{2N} s_{\mu}^2} \left(1 - \frac{E_t}{E_c} \right) \quad (D23)$$

$$G_{\mu\nu} = \frac{1}{64E_g s_{\mu}^2} \left[\delta_{\mu\nu} - \frac{E_t}{E_g} \frac{2c_{\mu} c_{\nu} o_{\mu} o_{\nu}}{Ns_{\nu}^2} \right] \quad (D24)$$

$$\text{where } E_t = \left(\frac{1}{E_c^1} + \sum_{n=0}^N \frac{1}{E_g^n} \right)^{-1}$$

Here G_{00} increases quadratically with a factor of $\left(1 - \frac{E_t}{E_c} \right)$. Thus, $G_{0\mu}$ is different from the parallel circuit by a factor $\left(1 - \frac{E_t}{E_c} \right)$. For the last term, $G_{\mu\nu}$, it is the same as parallel circuit because there is no term dependent on E_c .

d. *Linear Approximation* From here on, the sum over m, n runs from 1 to N while the sum over μ, ν runs from 1 to $N-1$. Simplification to including only linear terms from Taylor expansion of the cosine ($\cos x \sim 1 - \frac{x^2}{2}$) Eq. D19 and using $\sum_n W_{\mu m} W_{\nu m} = \delta_{\mu\nu}$, yields (upto a constant term)

$$\mathcal{U} = E_{J_p} \cos(\phi) - \frac{(\varphi_{-1} - \varphi_{-2})^2}{16E_{RO}} + \frac{E_{J_j}}{2N} \phi^2 + \frac{E_{J_j}}{2} \sum_{\mu} \xi_{\mu}^2 \quad (\text{D25})$$

$$= E_{J_p} \cos(\phi) + \frac{E_{J_j}}{2N} \phi^2 + \frac{E_{J_j}}{2} \sum_{\mu} \xi_{\mu}^2 - \frac{\varphi_-^2}{16E_{RO}}, \quad (\text{D26})$$

where $\dot{\phi}_{-1} = -\dot{\phi}_{-2} = eV$

e. *Hamiltonian*: We can see that there is no choice of $\dot{\varphi}_{\pm}$ such that the parasitic coupling between the readout resonator and fluxonium can be cancelled without eliminating the coupling between the qubit and readout resonator. Note that, this expression assumed $C_g^0 = C_g^N = C_g^{1..} = C_g^{N-1}$, such that $\frac{N+1}{E_g} = \frac{1}{E_g} - \frac{1}{E_c}$. The coupling between the qubit and the readout is same as the parallel circuit if $E_g \ll E_c$ with a lower N . We drive the readout resonator, such that, $\dot{\varphi}_- = 2eV$ (the sign of the voltage value has been changed because in this circuit φ_{-1} will be connected to V and not $-V$, just for simplicity). [SS: Check the sign of the eV terms]

$$\begin{aligned} \mathcal{L} = & \frac{\dot{\varphi}_+^2}{64E_c} \left(2 + \frac{(N+1)E_t}{E_g} \right) + \frac{\dot{\varphi}_+ eV}{16E_c} \left(\frac{3}{2} + \frac{E_t}{E_c} \right) \\ & - \frac{(N+1)E_t}{32E_g E_c} \dot{\phi} eV + \frac{(N+1)E_t}{64E_g E_c} \dot{\phi} \dot{\varphi}_+ \\ & - \frac{E_t}{16E_g E_c} \sum_{\mu} \frac{c_{\mu} o_{\mu}}{\sqrt{2N} s_{\mu}^2} \dot{\xi}_{\mu} eV \\ & + \frac{E_t}{32E_g E_c} \sum_{\mu} \frac{c_{\mu} o_{\mu}}{\sqrt{2N} s_{\mu}^2} \dot{\xi}_{\mu} \dot{\varphi}_+ \mathcal{O}(e^2 V^2) \\ & + \left[(M_{00} + G_{00}) \dot{\phi}^2 + 2 \sum_{\mu} (M_{0\mu} + G_{0\mu}) \dot{\phi} \dot{\xi}_{\mu} \right. \\ & \left. + \sum_{\mu, \nu} (M_{\mu\nu} + G_{\mu\nu}) \dot{\xi}_{\mu} \dot{\xi}_{\nu} \right] - \mathcal{U} \end{aligned} \quad (\text{D27})$$

This Lagrangian can be used to analyze effects in floating readout case. However, for simplicity, we can again just like the previous case, assume $C^3 = C^4 = 0$ which makes the floating resonator grounded. Ideally this choice should not affect the analysis until we study the effects of a driven readout resonator (even then the intuition is that the ground capacitance should not make things worse [SS: Check this intuition when analyzing a driven resonator. Also, we can check if changing $C_g^N = E_C^2 = E + C^1$ brings the effect of Floating resonator closer to a parallel circuit. It will never be similar because we have one less ground capacitance term here.]). Currently this is equivalent to eliminating all terms with E_c^3, E_c^4 and us-

ing $\dot{\varphi}_{-2} = 0, \dot{\varphi}_{-1} = -2eV$. Thus, $\varphi_+ = \varphi_- = -2eV$.

$$\begin{aligned} = & - \frac{(N+1)E_t}{16E_g E_c} \dot{\phi} eV - \frac{E_t}{8E_g E_c} \sum_{\mu} \frac{c_{\mu} o_{\mu}}{\sqrt{2N} s_{\mu}^2} \dot{\xi}_{\mu} eV \\ & + \left[(M_{00} + G_{00}) \dot{\phi}^2 + 2 \sum_{\mu} (M_{0\mu} + G_{0\mu}) \dot{\phi} \dot{\xi}_{\mu} \right. \\ & \left. + \sum_{\mu, \nu} (M_{\mu\nu} + G_{\mu\nu}) \dot{\xi}_{\mu} \dot{\xi}_{\nu} \right] - \mathcal{U} \end{aligned} \quad (\text{D28})$$

Next, we write the Legendre transformation using the velocity vectors and matrices,

$$\begin{aligned} p_{\phi} = \frac{\partial \mathcal{L}_{K_o}}{\partial \dot{\phi}} &= 2(M_{00} + G_{00}) \dot{\phi} + \sum_{\mu} (M_{\mu 0} + G_{\mu 0}) \dot{\xi}_{\mu} \\ & - \frac{(N+1)E_t}{16E_g E_c} eV \end{aligned} \quad (\text{D29})$$

$$\begin{aligned} p_{\xi_{\mu}} = \frac{\partial \mathcal{L}_{K_o}}{\partial \dot{\xi}_{\mu}} &= (M_{0\mu} + G_{0\mu}) \dot{\phi} + 2 \sum_{\nu} (M_{\mu\nu} + G_{\mu\nu}) \dot{\xi}_{\nu} \\ & - \frac{E_t}{8E_g E_c} \sum_{\mu} \frac{c_{\mu} o_{\mu}}{\sqrt{2N} s_{\mu}^2} eV \end{aligned} \quad (\text{D30})$$

Here, the even and odd sectors are not decoupled due to the eV term which will eventually act as the readout resonator mode. The even and odd sectors can be diagonalized independently, such that a rotation on the odd sectors does not affect the even sectors. This is contrary to the case of Eq. 77 in [26] where the rotation of odd sectors affects the even sectors. This is because in that case $G_{0\mu}$ was changed to being dependent on odd as well as even sectors. However, here, only the \mathcal{L}_V term has changed. Thus, if the following condition is satisfied,

$$\frac{\tilde{E}_c^{\phi} \tilde{E}_{c,j}^e c_i c_j}{32N E_g^2 s_i^2 s_j^2} \ll 1 \implies \frac{4E_g \tilde{E}_c^{\phi} c_i c_j}{32N E_g^2 s_i^2} \ll 1 \quad (\text{D31})$$

$$\implies \frac{4\tilde{E}_c^{\phi} N}{8E_g \pi^2 \mu\nu} \ll 1 \implies N \ll 8\pi^2 \frac{E_g}{\tilde{E}_c^{\phi}} \quad (\text{D32})$$

we can carry out the exact same procedure as Ref. [26] to simplify the inversion of matrix for the Legendre transformation and obtain the Hamiltonian as follows. [SS: Check both the matrix inverse requirement and condition in this case again]. Thus, we get the Hamiltonian as,

$$\begin{aligned} H_2 = & 4\tilde{E}_c^{\phi} p_{\phi}^2 + \sum_{\mu=1}^{N-1} 4\tilde{E}_{c,\mu}^{e/o} p_{\mu}^2 \\ & + 2 \sum_{\mu=1}^{N-1} \frac{\tilde{E}_c^{\phi} \tilde{E}_{c,\mu}^{e/o} c_{\mu} o_{\mu+1}}{\sqrt{2N} E_g s_{\mu}^2} p_{\phi} p_{\mu} \\ & - \tilde{E}_c^{\phi} p_{\phi} eV \left[\frac{(N+1)E_t}{2E_g E_c} + \frac{E_t \tilde{E}_{c,\mu}^{e/o}}{8E_g^2 E_c^2} \left(\frac{c_{\mu}^2 o_{\mu}}{2N s_{\mu}^4} \right) \right] \\ & - \sum_{\mu=1}^{N-1} \frac{\tilde{E}_c^{\phi} \tilde{E}_{c,\mu}^{e/o} c_{\mu} o_{\mu+1}}{\sqrt{2N} E_g s_{\mu}^2} \left[\frac{(N+1)E_t}{8E_g E_c} \right] p_{\mu} eV \\ & + E_{J_p} \cos \phi + \frac{E_L}{2} \phi^2 + \frac{E_{J_j}}{2} \sum_{\mu=1}^{N-1} \xi_{\mu}^2 - \frac{\varphi_-^2}{16E_{RO}} \end{aligned} \quad (\text{D33})$$

where the variables $\tilde{E}_{c,\mu}^e$ are same as before and $\tilde{E}_{c,\mu}^o$ is the diagonalized charging energy of odd sectors. $\tilde{E}_{c,\mu}^{e/o}$ denotes that the term will be $\tilde{E}_{c,\mu}^o$ for odd μ and $\tilde{E}_{c,\mu}^e$ for even μ . Thus, we can see that by not preserving the symmetry we only have the extra odd sector term interacting with the readout resonator. However, we can see that this term is extremely small. \mathcal{U} remains the same as the parallel case. Thus, in terms of types of couplings there might not be major differences, however, value of $\bar{E}_c^0 = (G_{00} + M_{00})^{-1}$ changes since G_{00} has changed. This change can also be diminished with increasing N . Thus, for large enough N , this circuit is the same as the parallel circuit. [SS: Write this in terms of previous format of H_ϕ]

3. Grounded Fluxonium Circuit: H_3

The constraint $\dot{\varphi}_N = 0$ yields

$$\mathcal{L} = \mathcal{L}_{\text{phase-slip}} + \mathcal{L}_{JJA} + \mathcal{L}_g + \mathcal{L}_{RO} + \mathcal{L}_C \quad (\text{D34})$$

$$\mathcal{L}_{\text{phase-slip}} = \frac{\dot{\varphi}_0^2}{16E_{C'}} - E_{J_p} \cos(\varphi_0 + \varphi_{\text{ext}}) \quad (\text{D35})$$

$$\mathcal{L}_{JJA} = \sum_{n=1}^N \frac{(\dot{\varphi}_n - \dot{\varphi}_{n-1})^2}{16E_{C_j}^n} - E_{J_j}^n \cos(\varphi_n - \varphi_{n-1}) \quad (\text{D36})$$

$$\mathcal{L}_{RO} = \frac{\dot{\varphi}_-^2}{16E_{RO}} - \frac{\varphi_-^2}{16E_{RO}} \quad (\text{D37})$$

$$\mathcal{L}_g = \sum_{n=0}^{N-1} \frac{\dot{\varphi}_n^2}{16E_g^n} \quad (\text{D38})$$

Here, we will not assume that the capacitances to transmission line are infinite or that ground capacitance for the phase-slip junction and JJA. We will leave the value of φ_\pm a variable in this case unlike the parallel circuit study we performed above. The grounding of fluxonium yields an additional condition to the fluxoid condition $\varphi_N = c$, a constant which implies,

$$\varphi_0 = c - \sum_{l=1}^N \theta_l \implies \dot{\varphi}_0 = - \sum_{l=1}^N \dot{\theta}_l \quad (\text{D39})$$

This used to be our qubit in the definition of collective modes in this article. However, in this case there are only $N - 1$ modes, such that the collective modes are defined as,

$$\phi = c + \sum_{l=1}^{N-1} \theta_l \implies \dot{\phi} = -\dot{\varphi}_0 \quad (\text{D40})$$

[SS: Is there a different mechanism we need to use here? (1) We should only have $N-1$ modes] Since one of the dynamic variables are fixed we only have $N - 1$

modes, thus,

$$\mathcal{L}_{\text{phase-slip}} = \frac{(\sum_{m=1}^{N-1} \dot{\theta}_m)^2}{16E_{C'}} + E_{J_p} \cos\left(\sum_{m=1}^N \theta_m + \varphi_{\text{ext}}\right) \quad (\text{D41})$$

$$\mathcal{L}_{JJA} = \sum_{n=1}^{N-1} \frac{\dot{\theta}_n^2}{16E_{C_j}^n} - E_{J_j}^n \cos \theta_n \quad (\text{D42})$$

$$\mathcal{L}_{RO} = \frac{(\dot{\varphi}_{-1} - \dot{\varphi}_{-2})^2}{16E_{RO}} - \frac{(\varphi_{-1} - \varphi_{-2})^2}{2L_{RO}} \quad (\text{D43})$$

$$\mathcal{L}_g = \frac{\dot{\varphi}_0^2}{16E_g^0} + \sum_{n=1}^N \frac{(\dot{\varphi}_0 + \sum_{m=1}^n \dot{\theta}_m)^2}{16E_g^n} \quad (\text{D44})$$

$$= \frac{\dot{\varphi}_0^2}{16E_g^0} + \sum_{n=1}^N \frac{1}{16E_g^n} (\dot{\varphi}_0^2 + 2\dot{\varphi}_0 \sum_{m=1}^n \dot{\theta}_m + \sum_{i=1}^n \sum_{j=1}^n \dot{\theta}_i \dot{\theta}_j) \quad (\text{D45})$$

$$= \dot{\varphi}_0^2 \sum_{n=0}^N \frac{1}{16E_g^n} + 2 \sum_{n=1}^N \sum_{m=1}^n \frac{\dot{\varphi}_0 \dot{\theta}_m}{16E_g^n} + \sum_{n=1}^N \sum_{j=1}^n \sum_{i=1}^n \frac{\dot{\theta}_i \dot{\theta}_j}{16E_g^n} \quad (\text{D46})$$

$$\begin{aligned} \mathcal{L}_c = & \frac{\dot{\varphi}_0^2}{16E_c^1} + \frac{\dot{\varphi}_{-1}^2}{16} \left(\frac{1}{E_c^1} + \frac{1}{E_c^3} \right) \\ & + \frac{\dot{\varphi}_{-2}^2}{16} \left(\frac{1}{E_c^4} + \frac{1}{E_c^2} \right) + \frac{(\dot{\varphi}_0 + \sum_{m=1}^N \dot{\theta}_m)^2}{16E_c^2} \\ & - \frac{\dot{\varphi}_0 \dot{\varphi}_{-1}}{8E_c^1} - \frac{\dot{\varphi}_{-1}(\dot{\varphi}_0 + \sum_{m=1}^N \dot{\theta}_m)}{8E_c^2} \\ & - \frac{\dot{\varphi}_{-2} eV}{8E_c^4} + \frac{\dot{\varphi}_{-1} eV}{8E_c^3} \end{aligned} \quad (\text{D47})$$

The term $\frac{(\dot{\varphi}_{-2})^2}{16E_c^4}$ will be added to the Lagrangian. The coupling constant for this case is,

$$\mathcal{L}_c = \frac{(\dot{\varphi}_{-1} - \dot{\varphi}_0)^2}{16E_c^1} + \frac{(\dot{\varphi}_{-1} - eV)^2}{16E_c^3} + \frac{(\dot{\varphi}_{-2})^2}{16E_c^4}, \quad (\text{D48})$$

$$\begin{aligned} \mathcal{L} = & \frac{\dot{\varphi}_+^2}{16E_c} \left(2 + \frac{NE_t}{E_g} \right) - \frac{\dot{\varphi}_+ eV}{4E_c} \left(\frac{3}{8} + \frac{E_t}{E_c} \right) \\ & - \frac{NE_t}{16E_g E_c} \dot{\phi} eV - \frac{NE_t}{32E_g E_c} \dot{\phi} \dot{\varphi}_+ \end{aligned} \quad (\text{D49})$$

$$\begin{aligned} & - \frac{E_t}{8E_g E_c} \sum_{\mu} \frac{c_{\mu} o_{\mu}}{\sqrt{2(N-1)} s_{\mu}^2} \dot{\xi}_{\mu} eV \\ & - \frac{E_t}{8E_g E_c} \sum_{\mu} \frac{c_{\mu} o_{\mu}}{\sqrt{2(N-1)} s_{\mu}^2} \dot{\xi}_{\mu} \dot{\varphi}_+ + \mathcal{O}(e^2 V^2) \end{aligned} \quad (\text{D50})$$

$$\begin{aligned} & + \left[(M_{00} + G_{00}) \dot{\phi}^2 + 2 \sum_{\mu} (M_{0\mu} + G_{0\mu}) \dot{\phi} \dot{\xi}_{\mu} \right. \\ & \left. + \sum_{\mu, \nu} (M_{\mu\nu} + G_{\mu\nu}) \dot{\xi}_{\mu} \dot{\xi}_{\nu} \right] - \mathcal{U} \end{aligned} \quad (\text{D51})$$

a. *Hamiltonian:* All terms in the Hamiltonian (H_2) can be adopted via $N \rightarrow N - 1$. If $C_g^N \neq C_g^1$ then this ground fluxonium and floating fluxonium have a larger difference in terms of frequencies of modes.

-
- [1] *Phys. Rev. X* **9**, 041041 (2019) - High-Coherence Fluxonium Qubit.
- [2] A. Somoroff, Q. Ficheux, R. A. Mencia, H. Xiong, R. Kuzmin, and V. E. Manucharyan, Millisecond Coherence in a Superconducting Qubit, *Physical Review Letters* **130**, 267001 (2023), publisher: American Physical Society.
- [3] Fluxonium: Single Cooper-Pair Circuit Free of Charge Offsets | Science.
- [4] N. Earnest, S. Chakram, Y. Lu, N. Irons, R. K. Naik, N. Leung, L. Ocola, D. A. Czaplewski, B. Baker, J. Lawrence, J. Koch, and D. I. Schuster, Realization of a Λ System with Metastable States of a Capacitively Shunted Fluxonium, *Physical Review Letters* **120**, 150504 (2018), publisher: American Physical Society.
- [5] H. Zhang, S. Chakram, T. Roy, N. Earnest, Y. Lu, Z. Huang, D. Weiss, J. Koch, and D. I. Schuster, Universal fast flux control of a coherent, low-frequency qubit, *Physical Review X* **11**, 011010 (2021), arXiv:2002.10653 [cond-mat, physics:quant-ph].
- [6] L. Ding, M. Hays, Y. Sung, B. Kannan, J. An, A. Di Paolo, A. H. Karamlou, T. M. Hazard, K. Azar, D. K. Kim, B. M. Niedzielski, A. Melville, M. E. Schwartz, J. L. Yoder, T. P. Orlando, S. Gustavsson, J. A. Grover, K. Serniak, and W. D. Oliver, High-Fidelity, Frequency-Flexible Two-Qubit Fluxonium Gates with a Transmon Coupler, *Physical Review X* **13**, 031035 (2023), publisher: American Physical Society.
- [7] H. Zhang, C. Ding, D. Weiss, Z. Huang, Y. Ma, C. Guinn, S. Sussman, S. P. Chitta, D. Chen, A. A. Houck, J. Koch, and D. I. Schuster, Tunable Inductive Coupler for High-Fidelity Gates Between Fluxonium Qubits, *PRX Quantum* **5**, 020326 (2024), publisher: American Physical Society.
- [8] K. N. Nesterov, C. Wang, V. E. Manucharyan, and M. G. Vavilov, cnot Gates for Fluxonium Qubits via Selective Darkening of Transitions, *Physical Review Applied* **18**, 034063 (2022), publisher: American Physical Society.
- [9] K. N. Nesterov, Q. Ficheux, V. E. Manucharyan, and M. G. Vavilov, Proposal for Entangling Gates on Fluxonium Qubits via a Two-Photon Transition, *PRX Quantum* **2**, 020345 (2021), publisher: American Physical Society.
- [10] E. Dogan, D. Rosenstock, L. Le Guevel, H. Xiong, R. A. Mencia, A. Somoroff, K. N. Nesterov, M. G. Vavilov, V. E. Manucharyan, and C. Wang, Two-Fluxonium Cross-Resonance Gate, *Physical Review Applied* **20**, 024011 (2023), publisher: American Physical Society.
- [11] E. L. Rosenfeld, C. T. Hann, D. I. Schuster, M. H. Matheny, and A. A. Clerk, *enDesigning high-fidelity two-qubit gates between fluxonium qubits*, Tech. Rep. arXiv:2403.07242 (arXiv, 2024) arXiv:2403.07242 [quant-ph] type: article.
- [12] *PRX Quantum* **3**, 037001 (2022) - Blueprint for a High-Performance Fluxonium Quantum Processor.
- [13] N. A. Masluk, I. M. Pop, A. Kamal, Z. K. Mineev, and M. H. Devoret, Microwave Characterization of Josephson Junction Arrays: Implementing a Low Loss Superinductance, *Physical Review Letters* **109**, 137002 (2012), publisher: American Physical Society.
- [14] F. Wang, K. Lu, H. Zhan, L. Ma, F. Wu, H. Sun, H. Deng, Y. Bai, F. Bao, X. Chang, R. Gao, X. Gao, G. Gong, L. Hu, R. Hu, H. Ji, X. Ma, L. Mao, Z. Song, C. Tang, H. Wang, T. Wang, Z. Wang, T. Xia, H. Xu, Z. Zhan, G. Zhang, T. Zhou, M. Zhu, Q. Zhu, S. Zhu, X. Zhu, Y. Shi, H.-H. Zhao, and C. Deng, *enAchieving millisecond coherence fluxonium through overlap Josephson junctions*, Tech. Rep. arXiv:2405.05481 (arXiv, 2024) arXiv:2405.05481 [quant-ph] type: article.
- [15] D. G. Ferguson, A. A. Houck, and J. Koch, Symmetries and collective excitations in large superconducting circuits, *Physical Review X* **3**, 011003 (2013).
- [16] A. Blais, A. L. Grimsmo, S. M. Girvin, and A. Wallraff, Circuit quantum electrodynamics, *Reviews of Modern Physics* **93**, 025005 (2021).
- [17] R. Shillito, A. Petrescu, J. Cohen, J. Beall, M. Hauru, M. Ganahl, A. G. Lewis, G. Vidal, and A. Blais, Dynamics of transmon ionization, *Physical Review Applied* **18**, 034031 (2022).
- [18] X. Xiao, J. Venkatraman, R. G. Cortiñas, S. Chowdhury, and M. H. Devoret, A diagrammatic method to compute the effective hamiltonian of driven nonlinear oscillators, arXiv preprint arXiv:2304.13656 (2023).
- [19] M. Khezri, A. Opremcak, Z. Chen, K. C. Miao, M. McEwen, A. Bengtsson, T. White, O. Naaman, D. Sank, A. N. Korotkov, *et al.*, Measurement-induced state transitions in a superconducting qubit: Within the rotating-wave approximation, *Physical Review Applied* **20**, 054008 (2023).
- [20] J. Cohen, A. Petrescu, R. Shillito, and A. Blais, Reminiscence of classical chaos in driven transmons, *PRX Quantum* **4**, 020312 (2023).
- [21] M. F. Dumas, B. Groleau-Paré, A. McDonald, M. H. Muñoz-Arias, C. Lledó, B. D'Anjou, and A. Blais, Unified picture of measurement-induced ionization in the transmon, arXiv preprint arXiv:2402.06615 (2024).
- [22] D. Sank, Z. Chen, M. Khezri, J. Kelly, R. Barends, B. Campbell, Y. Chen, B. Chiaro, A. Dunsworth, A. Fowler, *et al.*, Measurement-induced state transitions in a superconducting qubit: Beyond the rotating wave approximation, *Physical review letters* **117**, 190503 (2016).
- [23] K. N. Nesterov and I. V. Pechenezhskiy, Measurement-induced state transitions in dispersive qubit readout schemes, arXiv preprint arXiv:2402.07360 (2024).
- [24] L. B. Nguyen, Y.-H. Lin, A. Somoroff, R. Mencia, N. Grabon, and V. E. Manucharyan, High-coherence fluxonium qubit, *Physical Review X* **9**, 041041 (2019).
- [25] V. E. Manucharyan, J. Koch, L. I. Glazman, and M. H. Devoret, Fluxonium: Single cooper-pair circuit free of charge offsets, *Science* **326**, 113 (2009).
- [26] G. Viola and G. Catelani, Collective modes in the fluxonium qubit, *Physical Review B* **92**, 224511 (2015).
- [27] D. Gusenkova, M. Spiecker, R. Gebauer, M. Willsch, D. Willsch, F. Valenti, N. Karcher, L. Grünhaupt, I. Takmakov, P. Winkel, *et al.*, Quantum nondemolition dispersive readout of a superconducting artificial atom using large photon numbers, *Physical Review Applied* **15**, 064030 (2021).
- [28] G. Zhu, D. G. Ferguson, V. E. Manucharyan, and J. Koch, Circuit QED with fluxonium qubits: Theory of the dispersive regime, *Physical Review B* **87**,

- 024510 (2013), publisher: American Physical Society.
- [29] T. N. Ikeda, S. Tanaka, and Y. Kayanuma, Floquet-landau-zener interferometry: Usefulness of the floquet theory in pulse-laser-driven systems, *Physical Review Research* **4**, 033075 (2022).
 - [30] N. A. Masluk, *Reducing the losses of the fluxonium artificial atom* (Yale University, 2013).
 - [31] A. G. Fowler, M. Mariantoni, J. M. Martinis, and A. N. Cleland, Surface codes: Towards practical large-scale quantum computation, *Physical Review A—Atomic, Molecular, and Optical Physics* **86**, 032324 (2012).
 - [32] S. Hazra, W. Dai, T. Connolly, P. Kurilovich, Z. Wang, L. Frunzio, and M. Devoret, Benchmarking the readout of a superconducting qubit for repeated measurements, *arXiv preprint arXiv:2407.10934* (2024).
 - [33] Z. Huang, P. S. Mundada, A. Gyonis, D. I. Schuster, A. A. Houck, and J. Koch, enEngineering Dynamical Sweet Spots to Protect Qubits from 1/\$f\$ Noise, *Physical Review Applied* **15**, 034065 (2021), *arXiv:2004.12458 [quant-ph]*.
 - [34] M. D. Reed, L. DiCarlo, B. R. Johnson, L. Sun, D. I. Schuster, L. Frunzio, and R. J. Schoelkopf, High-Fidelity Readout in Circuit Quantum Electrodynamics Using the Jaynes-Cummings Nonlinearity, *Physical Review Letters* **105**, 173601 (2010), publisher: American Physical Society.
 - [35] M. H. Muñoz-Arias, C. Lledó, and A. Blais, Qubit readout enabled by qubit cloaking, *Physical Review Applied* **20**, 054013 (2023), publisher: American Physical Society.
 - [36] N. Didier, J. Bourassa, and A. Blais, Fast Quantum Nondemolition Readout by Parametric Modulation of Longitudinal Qubit-Oscillator Interaction, *Physical Review Letters* **115**, 203601 (2015), publisher: American Physical Society.
 - [37] J. Gambetta, A. Blais, D. I. Schuster, A. Wallraff, L. Frunzio, J. Majer, M. H. Devoret, S. M. Girvin, and R. J. Schoelkopf, Qubit-photon interactions in a cavity: Measurement-induced dephasing and number splitting, *Physical Review A* **74**, 042318 (2006).
 - [38] A. Clerk and D. W. Utami, Using a qubit to measure photon-number statistics of a driven thermal oscillator, *Physical Review A—Atomic, Molecular, and Optical Physics* **75**, 042302 (2007).
 - [39] Alternatively, for the coupling strengths with readout, we multiply with the constant factor of $\frac{1}{2\pi}\omega_r\sqrt{\frac{\pi Z}{R_K}}\approx 1$ in GHz for (eV/h), where $R_K = h/e^2 = 25.8K\Omega$, $Z = 50 * 4/\pi\Omega$, $\omega_r \approx 10\text{GHz}$. Thus, $eVZPF/h = 0.14$ which can be checked against $n_{ZPF,r}$ quoted for chip 2(A&B) as follows. $n = Q/2e = CV/2e = (eV/h)/\omega_r * Z_r * 2e^2/h = 0.14/(2\omega_r * Z_r/R_K) = 2.84$.
 - [40] G. Catelani, R. J. Schoelkopf, M. H. Devoret, and L. I. Glazman, Relaxation and frequency shifts induced by quasiparticles in superconducting qubits, *Physical Review B* **84**, 064517 (2011).
 - [41] J. Koch, V. Manucharyan, M. Devoret, and L. Glazman, Charging effects in the inductively shunted josephson junction, *Physical review letters* **103**, 217004 (2009).